

See discussions, stats, and author profiles for this publication at: <https://www.researchgate.net/publication/241691800>

Multifunctional calcium phosphate nano-contrast agent for combined nuclear, magnetic and near-infrared invivo imaging

ARTICLE in BIOMATERIALS · JUNE 2013

Impact Factor: 8.56 · DOI: 10.1016/j.biomaterials.2013.05.077 · Source: PubMed

CITATIONS

10

READS

86

9 AUTHORS, INCLUDING:



Anusha Ashokan

Amrita Institute of Medical Sciences and Re...

6 PUBLICATIONS 151 CITATIONS

[SEE PROFILE](#)



G Siddaramana Gowd

Amrita Vishwa Vidyapeetham

13 PUBLICATIONS 216 CITATIONS

[SEE PROFILE](#)



Vijay Harish Somasundaram

Amrita Vishwa Vidyapeetham

11 PUBLICATIONS 14 CITATIONS

[SEE PROFILE](#)

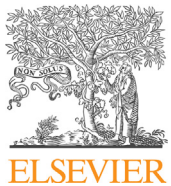


Arun Bhupathi

Vishnu Dental College

9 PUBLICATIONS 26 CITATIONS

[SEE PROFILE](#)



Multifunctional calcium phosphate nano-contrast agent for combined nuclear, magnetic and near-infrared *in vivo* imaging

Anusha Ashokan^a, Genekehal S. Gowd^a, Vijay H. Somasundaram^{a,c}, Arun Bhupathi^a, Reshma Peethambaran^b, A.K.K. Unni^b, Shanmugasundaram Palaniswamy^c, Shantikumar V. Nair^a, Manzoor Koyakutty^{a,*}

^a Amrita Centre for Nanosciences and Molecular Medicine, Amrita Institute of Medical Sciences and Research Centre, Cochin 682041, Kerala, India

^b Central Lab Animal Facility, Amrita Institute of Medical Science and Research Centre, Cochin 682041, Kerala, India

^c Department of Nuclear Medicine, Amrita Institute of Medical Science and Research Centre, Cochin 682041, Kerala, India

ARTICLE INFO

Article history:

Received 20 May 2013

Accepted 30 May 2013

Available online 21 June 2013

Keywords:

Calcium phosphate nanoparticles

NIR contrast

Magnetic contrast

Nuclear contrast

Tri-modal *in vivo* imaging

ABSTRACT

Combination of three imaging techniques such as nuclear, magnetic and near-infrared fluorescence can aid in improved diagnosis of disease by synergizing specific advantages of each of these techniques such as deep tissue penetration of radiation signals, anatomical and functional details provided by magnetic contrast and better spatial resolution of optical signals. In the present work, we report the development of a multimodal contrast agent based on calcium phosphate nanoparticles (nCP), doped with both indocyanine green (ICG) and Gadolinium (Gd^{3+}), and labeled with ^{99m}Tc -MDP for combined optical, magnetic and nuclear imaging. In order to obtain the desired tri-modal contrast properties, the concentrations of ICG, Gd^{3+} and ^{99m}Tc were optimized at ~0.15 wt%, 3.38 at% and ~0.002 ng/mg of nCP, respectively. The leaching-out of ICG was protected by an additional coating of polyethyleneimine (PEI). Toxicological evaluation of the final construct carried out on healthy human mononuclear cells, red-blood cells and platelets, showed excellent hemocompatibility. *In vivo* multimodal imaging using mice models revealed the ability to provide near-infrared, magnetic and nuclear contrast simultaneously. The nanoparticles also showed the potential for improved MR based angio-imaging of liver. Retention of intravenously administrated nanoparticles in the liver was reduced with PEGylation and the clearance was observed within 48 h without causing any major histological changes in vital organs. Thus, we developed a non-toxic tri-modal nano-contrast agent using calcium phosphate nanoparticles and demonstrated its potential for combined nuclear, magnetic and near-infrared imaging *in vivo*.

© 2013 Elsevier Ltd. All rights reserved.

1. Introduction

Development of nanoparticle-based multimodal contrast agents is gaining great interest in the field of diagnosis and therapy [1–4]. Multimodal imaging is a technique where two or more imaging modalities are combined to obtain specific advantages of various methods simultaneously. For example, combining physiological characteristics provided by techniques such as positron emission tomography (PET) or single photon emission tomography (SPECT) with anatomical and molecular details provided by computed tomography (CT) and magnetic resonance imaging (MRI) has great potential in disease diagnosis, treatment planning and prognosis

analysis [5,6]. So far, there has been significant progress in the area of developing combined PET–CT, PET–MRI and SPECT–MRI systems [7,8]. Compared to CT, MRI has specific advantageous due to the non-ionizing means of imaging, much better soft tissue contrast, physiological and functional imaging capabilities, diffusion weighted imaging or dynamic contrast enhanced imaging modes that can help in detecting metastasis to lymph nodes and specific amino acid profiles [9]. Further, if we can combine PET–MRI or SPECT–MRI with near-infrared (NIR) fluorescence imaging, it will be possible to conduct image guided surgical procedures by correlating the PET/SPECT and MRI data with intra-operative NIR images [10].

In the present clinical practice, each of these imaging modalities needs separate contrast agents such as Fluorine-18 fluorodeoxyglucose (^{18}F -FDG) for PET, ^{99m}Tc for SPECT, 2-gadolinium diethylenetriamine-pentaacetic acid (Gd –DTPA) for

* Corresponding author. Fax: +91 (0) 484 280 2020.

E-mail addresses: manzoork@aims.amrita.edu, manzoork@gmail.com (M. Koyakutty).

MRI and Indocyanine green (ICG) for optical imaging. The pharmacokinetic profiles of each of these contrast agents differ significantly and getting them simultaneously to a particular diseased site for combinatorial imaging is a major challenge. In addition, simultaneous use of multiple contrast agents may increase the risk of cumulative toxicity. Ideally, this issue can be overcome by developing a single contrast agent that can provide multiple contrast properties together with biocompatibility. With the emergence of nanotechnology, there have been serious efforts in developing multimodal contrast agents using polymers, lipids, liposomes, inorganic particles [11–15]. Most of the reports are based on developing nanoparticles for combined magnetic and optical imaging, where a magnetic core (mostly iron oxide) is either surrounded by a fluorescent quantum dot shell (CdSe, CdTe) or embedded in a nanoparticle co-loaded with fluorescent dyes [16,14]. Recently, Jokerst et al. reported on the application of Gd³⁺ and FITC loaded silica nanoparticles for ultrasound guided stem cell implantation and MRI based long term cell tracking [15]. The toxicity of CdSe, CdTe quantum dots [17] as well as silica like materials [18] and the aggregation of organic dyes within nanoparticles leading to fluorescent quenching [19] are the major limitations of such systems. Nanoparticles combining optical and nuclear imaging modalities are also being developed [20–22]. Generally, optical and nuclear contrast moieties were conjugated to reactive carboxyls or amines in chelates such as tetraazacyclododecane–tetra acetic acid (DOTA) or peptides [20,23]. In addition to bimodal contrast agents, recently, tri-modal agents were also developed for combined optical, nuclear and magnetic contrast imaging [24]. Xie et al. reported an FeO based tri-modal agent [24] labeled with Cy5.5 and ⁶⁴Cu-DOTA where the radio-labeling efficiency varied from 5 to 88% [25]. In another report, an aptamer conjugated cobalt ferrite nanoparticle surrounded by rhodamine within a silica shell labeled with ⁶⁷Ga citrate was reported [26]. Both the above works used iron oxide nanoparticle which is a *T*₂ contrast agent giving dark contrast which may be confused with bleeding, calcification and susceptibility artifacts compared to *T*₁ agents based on Gd³⁺ [27]. In another interesting work, ¹⁸F-labeled lanthanide doped NaYF4 nano-phosphors were reported for combined nuclear, magnetic and up-conversion luminescent properties [28]. In addition to low up-conversion quantum yield of NaYF4, the biocompatibility of rare-earth fluorides is not well understood.

Recently, the application of calcium phosphate nanoparticles for the development of diagnostic [29,30], drug [31], gene [32] or siRNA [33] delivery agents is being widely researched upon. Calcium phosphate, being the mineral component of human bone and teeth, is an appropriate choice for the development of non-toxic contrast agents. It is used clinically for bone tissue regeneration and as adjuvant for vaccines [34,35]. Barth et al. reported development of ICG doped calcium phosphosilicate nanoparticles for targeted *in vivo* NIR imaging of breast and pancreatic tumor [36] as well as for photodynamic therapy of leukemia in mice models [37]. Calcium phosphosilicate nanoparticles had an improved ICG loading efficiency and quantum yield compared to polymeric nanoparticles [29]. In our earlier study, we reported on the development of Eu³⁺ and Gd³⁺ doped hydroxyapatite nanoparticles (nHAp) for combined optical, magnetic and X-ray contrast imaging [38]. Chen et al., also reported the development of Eu³⁺ and Gd³⁺ doped calcium phosphate nanospheres and hydroxyapatite nanorods for multimodal imaging together with drug delivery [39,40]. But the emission of Eu³⁺ was not in the NIR range that was suitable for *in vivo* imaging. Considering this limitation we have doped NIR emitting dye, ICG, into nHAp [41].

In the present work, we report a tri-modal contrast agent based on calcium phosphate nanoparticles for combined optical, magnetic

and nuclear imaging and demonstrated its *in vivo* application using mouse models. Calcium phosphate nanoparticles (nCP) were doped with ICG and Gadolinium (Gd³⁺) and surface labeled with ^{99m}Tc-MDP such that all the three contrast properties could be derived from a single nanoparticle. To the best of our knowledge, this is the first report on tri-modal contrast agent based on calcium phosphate nanoparticles for combined near-infrared, magnetic and nuclear imaging. In further discussions we refer this tri-modal contrast agent as multifunctional nCP (MF-nCP). We have discussed the optimization of various synthesis parameters to obtain the best tri-modal contrast properties *in vivo*. The effect of polyethylene glycol (PEG) capping on biodistribution is also discussed.

2. Materials and methods

2.1. Synthesis of MF-nCP

All the precursors were prepared in endotoxin free water and the synthesis was carried out under highly sterile conditions. In a typical reaction procedure, 20 mL of 0.05 M calcium chloride (CaCl₂, Sigma, USA) was mixed with 20 mL 0.01 M trisodium citrate, 1 mM ICG (Sigma, USA) and 0.1 M Gadolinium nitrate (Gd(NO₃)₃) for 30 min at room temperature (~25 °C). Volume of ICG taken was varied from 15 μL to 72 μL that corresponded to weight % of ICG to calcium phosphate ranging from 0.05 to 0.24% (total yield of undoped calcium phosphate was 30 mg). Volume of Gd(NO₃)₃ was varied from 150 μL to 2.5 mL that corresponded to Gd atomic % varying from 1.5 to 25% (wrt Ca). Later, the effective Gd³⁺ doping was characterized by Inductively Coupled Plasma-Atomic Emission Spectroscopy (ICP-AES). Then, 5 mL of 0.03 M diammonium hydrogen phosphate ((NH₄)₂HPO₄, S.D. Fine Chemicals, India) mixed with 2 mL of 3 N ammonium hydroxide (NH₄OH) was added drop wise to CaCl₂-ICG-Gd³⁺ mixture under constant stirring to obtain ICG and Gd³⁺ doped calcium phosphate nanoparticles (ICG-Gd-nCP). The precipitate was washed and dispersed in 30 mL endotoxin free water. 40 mL of 0.00025 weight% polyethyleneimine (PEI) (average molecular weight 25,000, Sigma, USA) was added to the ICG-Gd-nCP and stirred for 30 min to obtain PEI capped ICG-Gd-nCP. The pH during the entire process was maintained at ~9 by NH₄OH. The precipitate was then centrifuged at 6000 rpm for 3 min and washed with endotoxin free water at least two times. Next, conjugation of ^{99m}Tc-MDP to the prepared ICG-Gd-nCP was to be carried out. ^{99m}Tc-MDP conjugate was prepared by adding ^{99m}Tc (sodium pertechnetate solution) to the MDP cold-kit (Board of Radiation and Isotope Technology, India. Kit contents: Methylene diphosphonate – 10 mg, tin(II) chloride dehydrate – 1 mg, ascorbic acid – 1.8 mg) and incubating at room temperature for 10 min. A labeling efficiency of >95% was ensured by chromatographic analysis. Different volumes of ^{99m}Tc-MDP (radioactivity ranging from 60 to 300 μCi) was treated with 1 mL of ICG-Gd-nCP (20 mg/mL) and allowed to stand at room temperature for 30 min. After incubation, the sample was washed twice to remove unconjugated radionuclide to obtain MF-nCP. Radioactivity of the conjugates and the supernatants obtained on washing steps were measured in a radionuclide dose calibrator (Capintec, USA). Radiation protection techniques were practiced while handling the radioactive material.

Polyethylene glycol capping (PEGylation) of MF-nCP was carried out using N hydroxysuccinimide (NHS) activated branched PEG molecules (molecular weight 40,000, Jenkem technology, USA). 1 mg/mL of MF-nCP dispersed in phosphate buffered saline (PBS – pH 7.4) was treated with 13 μL of 15 mM NHS-PEG at 4 °C for 2 h. The conjugated sample was then washed in PBS twice in order to obtain the final sample.

2.2. Characterization of MF-nCP

Crystallinity of MF-nCP was studied by X-ray powder diffraction using PANalytical X Pert-pro system fitted with Cu-Kα source. Composition of the material was characterized by Fourier Transform Infrared (FTIR) spectra of KBr supported samples using PerkinElmer Spectrum RX1. The particle size analysis was carried out using Scanning electron microscope (SEM) [JEOL JSM-6490 LA] and dynamic light scattering (Nano ZS, Zetasizer Nanoseries, Malvern). Zeta potential of the sample was measured using Nano ZS, Zetasizer Nanoseries, Malvern. Fluorescence excitation and emission spectra of 1 mg/mL of sample were recorded using HORIBA-JOBINYVON Fluoromax 4 Spectrofluorometer. NIR fluorescence imaging of samples were carried out in a multispectral imaging station (Kodak Multispectral *in vivo* imaging system FX pro, USA) using a band pass excitation filter of 760 ± 15 nm and an emission filter of 830 ± 15 nm. 100 μL of 5 mg/mL of each sample was taken in a 96 well plate and imaged for an exposure time of 30 s. A fixed region of interest (ROI) was chosen for each sample and the average fluorescence intensity over the ROI was analyzed for fluorescence intensity comparison between different samples. To study the effect of different capping agents, 100 μL of the supernatants collected after each washing step of capped samples was analyzed and their fluorescence intensity was compared.

Quantitative evaluation of the efficiency of Gd³⁺ doping was carried out using ICP-AES (Thermo Electron IRIS INTREPID II XSP DUO), for which doped nCP was

dissolved in 10% nitric acid. MRI of samples was carried out in a 7 T animal MRI station (Bruker BioSpec, USA). Different concentration nCP was dispersed in 1% agar and taken in small tubes. T_1 based MR contrast imaging was carried out using T_1 FLASH imaging sequence with TR = 8.5 ms, TE = 2.2, FA = 15°. For measuring r_1 relaxivity, T_1 mapping sequence was carried out for different concentrations of the material. The slope of the $1/T_1$ vs concentration of Gd^{3+} was calculated for obtaining the relaxivity value.

In order to image radioactive emission from MF-nCP, 100 μ L of 20 mg/mL of the sample conjugated to varying concentrations of ^{99m}Tc -MDP and washed, were taken in a 96 well plate and imaged for an exposure time of 30 s with a resolution of 4 \times 4 pixels (Kodak Multispectral *in vivo* imaging system FX pro, USA). The radioactive emissions are collected on a radiographic phosphor plate to produce light emission which is then recorded by a charge coupled device. The radioactivity of the MF-nCP samples was further quantified using radionuclide dose calibrator (Capintec, US) as

absorbance was measured at 570 and 600 nm. Cell viability in the PBS control was taken as 100% for percentage viability calculation.

2.4.2. Hemolysis analysis

Soret band based absorption of free hemoglobin in blood plasma at 415 nm was used for the analysis of hemolytic potential of nanoparticles. Whole blood was collected into 3.8% trisodium citrate anticoagulant (volume ratio of anticoagulant to blood = 1:9). 450 μ L of whole blood was treated with 50 μ L of MF-nCP samples for 3 h at 37 °C under mild mixing condition. PBS and 1% Triton X-100 served as negative and positive control respectively. The treated blood was then centrifuged at 4000 rpm for 15 min. The plasma was then collected and diluted with 0.01% sodium carbonate. Absorbance was measured spectrophotometrically (UV-1700, Shimadzu) at 380, 415 and 450 nm. Amount of plasma hemoglobin was calculated as in Equation (1).

$$\text{Amount of plasma hemoglobin (mg/dL)} = \frac{2 \times A_{415} - (A_{380} + A_{450}) \times 1000 \times \text{Dilution factor}}{(E \times 1.655)} \quad (1)$$

well as by drawing regions of interest (ROI) around the sites showing radiotracer activity in the images obtained in a gamma camera and estimating the intensity of the signal within each ROI. Conjugation of 0.04 ng of ^{99m}Tc -MDP to 20 mg ICG-Gd-nCP was confirmed by paper chromatography. ^{99m}Tc -MDP treated ICG-Gd-nCP sample (without washing) was spotted at a distance of ~1 cm from one edge of a strip of No: 3 Whatman paper (15 cm in length). This was dried by suspending in air for 10–15 min. The paper strip was suspended vertically into the chromatography jar containing saline, such that the edge of the strip closest to the drop was just immersed in the saline. It was suspended until the solvent ran up to two third length of the strip following which it was removed and dried. The strips were imaged for both fluorescence and radioactive emission using multispectral imaging station (Kodak Multispectral *in vivo* imaging system FX pro, USA). The stability of ^{99m}Tc -MDP conjugation to ICG-Gd-nCP was studied by running paper chromatogram at different time intervals. MF-nCP was incubated in PBS over a period of 9 h and paper chromatography was carried out at the 0th and 9th hour. Imaging of the chromatogram was done for nuclear contrast (Kodak Multispectral *in vivo* imaging system FX pro, USA) as the radioactivity was too low to be measured in radionuclide dose calibrator.

2.3. Tri-modal imaging using MF-nCP

MF-nCP was dispersed in 1% agar at a concentration of 3 mg/mL, taken in a small tube and imaged for NIR, magnetic and nuclear contrast. NIR, X-ray and nuclear contrast imaging was carried out in the multispectral imaging station (Kodak Multispectral *in vivo* imaging system FX pro, USA) and MRI was done using 7 T animal MRI (Bruker) under the same *in vitro* imaging conditions mentioned in Section 2.2. *Ex situ* tissue imaging experiments were carried out using porcine tissue. The tissue was taken in a cylindrical container. ~2 mg of MF-nCP was placed at a depth of 2 cm within the pork tissue. Fluorescence (band pass filters – excitation filter: 760 ± 15 nm, emission filter: 830 ± 15 nm), X-ray and radioisotope imaging was carried out in a multispectral imaging station (Kodak Multispectral *in vivo* imaging system FX pro, USA). Radioactive emission images were overlaid on the corresponding X-ray images. An exposure time of 1 min and 2 min were used for fluorescence and radioisotope imaging respectively. Magnetic contrast imaging was carried out in a 7T animal MRI station (Bruker BioSpec, USA) with TE = 2.2 ms, TR = 80 ms, FA = 50°, Number of averages = 15.

2.4. Hematotoxicological evaluation

Hemocompatibility analysis was carried out in human peripheral blood samples collected from healthy volunteers after the approval of the ethical committee at Amrita Institute of Medical Science and Research center (AIMS), Kerala, India. All the experiments were repeated with 3 independent donor samples.

2.4.1. Cytotoxicity analysis

Cytotoxicity of MF-nCP toward peripheral blood derived mononuclear cells (PBMC) was analyzed using Alamar blue assay. PBMC were isolated from whole blood using density gradient separation using Histopaque 1077, density 1.077 g/mL (Sigma, USA). The cells were collected, washed and redispersed in RPMI complete medium containing 10% FBS, 2 mM L-glutamine and 50 μ M β mercaptoethanol. 100 μ L of MF-nCP of concentrations varying from 20 to 500 μ g/mL, were taken in 96 well plates. 100 μ L of cells at a concentration of 10^5 cells/mL were seeded into the wells containing the samples. PBS served as the negative control and Triton X-100 served as the positive control for the experiment. The cells were then incubated at 37 °C for 72 h. 100 μ L of 10% (volume) Alamar blue was added and incubated for 8 h before the

where A_{415} , A_{380} , A_{450} are the absorbance values at 415, 380 and 450 nm. A_{415} is the soret band based absorption of hemoglobin. A_{380} and A_{450} are correction factors applied for uroporphyrin absorption. E is molar absorptivity value of oxyhemoglobin at 415 nm ($E = 79.46$). 1.655 is the correction factor applied due to the turbidity of plasma sample. % Hemolysis was calculated as in Equation (2).

$$\% \text{ Hemolysis} = \frac{\text{Plasma Hb value of sample}}{\text{Total Hb value of blood}} \times 100 \quad (2)$$

For SEM imaging, RBC after nanoparticle treatment was incubated with 2.5% glutaraldehyde for 30 min. The cells were then washed twice in PBS and SEM imaging was done.

2.4.3. Platelet activation study

Whole blood was collected from healthy volunteers and added to 3.8% trisodium citrate anticoagulant (volume ratio of anticoagulant to blood = 1:9). Blood was then centrifuged at 150 g for 10 min at 19 °C for the collection of platelet rich plasma (PRP). PRP was then diluted 10 times with sterile filtered PBS and equilibrated at 37 °C for 30 min. 50 μ L of MF-nCP sample was treated with 450 μ L of the diluted PRP for 20 min. PBS and 50 μ M ADP (Adenosine diphosphate) (Sigma, USA) served as negative and positive controls respectively. Treatment of ADP with PRP was done for only 5 min. 100 μ L of this PRP was incubated with 20 μ L of PerCP-Cy5 labeled CD62P (BD bioscience, India) and FITC labeled CD42b (BD bioscience, India) antibodies for 20 min in dark at room temperature. The samples were then washed once with PBS, resuspended in 1 mL PBS and analyzed immediately by flow cytometry (FACS Aria™). Isotype controls of IgG1k PerCP-Cy5 and IgG1k FITC were used.

2.5. *In vivo* imaging experiments

Adult Swiss albino mice of average weights ~20 g were used for *in vivo* multimodal imaging experiments. Animals were obtained from Central Animal Lab facility, AIMS after the approval from Animal Ethical Committee at AIMS. The animals were maintained individually in cages at a temperature of 20 ± 2 °C with 12 h light-12 h darkness cycle. The animals were fed on corn and glucose diet for 48 h prior to the experiment in order to avoid any interference from auto-fluorescence of their regular feed. Ventral side of the mice was completely shaved before the imaging experiments to avoid fluorescence from fur. 100 μ L of the MF-nCP sample was injected at a dose of 10 mg/kg through tail vein. The total radioactivity of the sample injected was measured to be ~20 μ Ci. Imaging was done using *in vivo* multispectral imaging station (Kodak Multispectral *in vivo* imaging system FX pro, USA). For fluorescence imaging, an excitation band pass filter of 760 ± 15 nm and emission band pass filter of 830 ± 15 nm with an exposure time of 2 min was used. Radiolabel imaging was done for an exposure time of 6 min with an image resolution of 4 \times 4 pixels. For each radioactive emission image, a corresponding 30 s X-ray image was taken. The nuclear contrast image was then overlaid on the X-ray image for identification of the exact location of the nuclear contrast. Imaging was done at different time intervals ranging from 5 min to 48 h post sample injection.

For *in vivo* MRI experiments, mice were anesthetized in an induction chamber of isofluorane–oxygen mixture (5% isofluorane) and then placed on an animal bed with a mask providing continuous flow of the anesthesia (maintenance dose – 2% isofluorane). A respiration pad and temperature probe with circulating warm water was used to continuously monitor and maintain respiration rate and body temperature (~37 °C). For T_1 based MR contrast imaging, a T_1 FLASH imaging sequence with TR = 80 ms, TE = 2.2 ms, FA = 50° was carried out. For MR angiogram of liver region, FLASH-TOF-2D-Flow Comp sequence with TE/TR = 3.5/12.014 ms, NEX-5, FA 80°, was used for an FOV covering the liver region. After imaging experiments were

completed, the experimental animals were euthanized by an overdose of the anesthetic (Xylazine:Ketamine = 1:4). Organs were then collected and imaged for fluorescence and radioactive emission. In order to quantify fluorescence from each organ, the entire organ was chosen as ROI and the average fluorescence intensity was recorded. Soon after ex-vivo imaging, all organs were fixed in 10% formalin solution for histological evaluation. Organs were embedded in paraffin wax blocks, 5 μm thick sections were made on glass slides and stained with hematoxylin and eosin. After completing the standard staining protocol, sections were micrographed under 10 \times and 40 \times magnifications.

3. Results and discussion

3.1. Synthesis and characterization of MF-nCP

An aqueous wet chemical synthesis route was optimized for the synthesis of MF-nCP. ICG and Gd³⁺ were doped within nCP by precipitation of calcium chloride and diammmonium hydrogen phosphate in the presence of ICG and Gd(NO₃)₃ in an aqueous medium. Different parameters were optimized for effective loading of the dopants within the nanoparticles as well as for controlling the particle size. In order to find out the best possible method for doping, we have attempted 3 different routes: (i) mixing of ICG and Gd(NO₃)₃ with Ca²⁺ precursor before drop wise addition of (PO₄)³⁻ precursor (ii) mixing of ICG and Gd(NO₃)₃ with (PO₄)³⁻ precursor and drop wise addition to Ca²⁺ precursor (iii) separate addition of ICG, Gd(NO₃)₃ and (PO₄)³⁻ precursor to Ca²⁺ precursor. Among the sequences mentioned above, method (i) proved to be more efficient for the co-doping of ICG dye and Gd³⁺ within nCP. This may be due

to the charge-based interaction between negatively charged sulphonate groups in ICG and the positively charged Ca²⁺ and Gd³⁺ ions.

For controlling the size of apatite nanoparticles, pH of the reaction medium was an important parameter as discussed in our previous reports [38,41]. Typically, in slightly acidic-neutral pH of 5–7, elongated rod shaped crystals were formed whereas in alkaline pH ~ 9, the resulting nanoparticles were spherical with an average size ~ 80 nm. Accordingly in the present work, pH of reaction mixture was maintained at ~9 by the addition of NH₄OH, resulting in the formation of MF-nCP of average size ~ 80 nm. Precipitation in the presence of citrate also prevented the aggregation of nCP in to larger particles. The role of citrate in controlling the growth of hydroxyapatite/calcium phosphate is well reported [42,43]. The concentration of trisodium citrate required to prevent the aggregation or crystallization of ICG-Gd-nCP into larger particles was optimized by synthesizing ICG-Gd-nCP in varying concentrations of trisodium citrate. The size of the precipitated ICG-Gd-nCP was observed through microscope (data not shown). It was found that, concentration of trisodium citrate needed to be one fifth of the calcium precursor, in order to prevent agglomeration. Another major challenge associated with ICG-Gd-nCP was the leaching-out of ICG from the nanoparticles during washing. Different capping agents such as inorganic silica and polymers such as PEG and PEI were investigated for its efficiency to contain ICG within the nanoparticles as discussed in Section 3.2. PEI proved to be the most efficient capping agent to prevent leaching of the dye

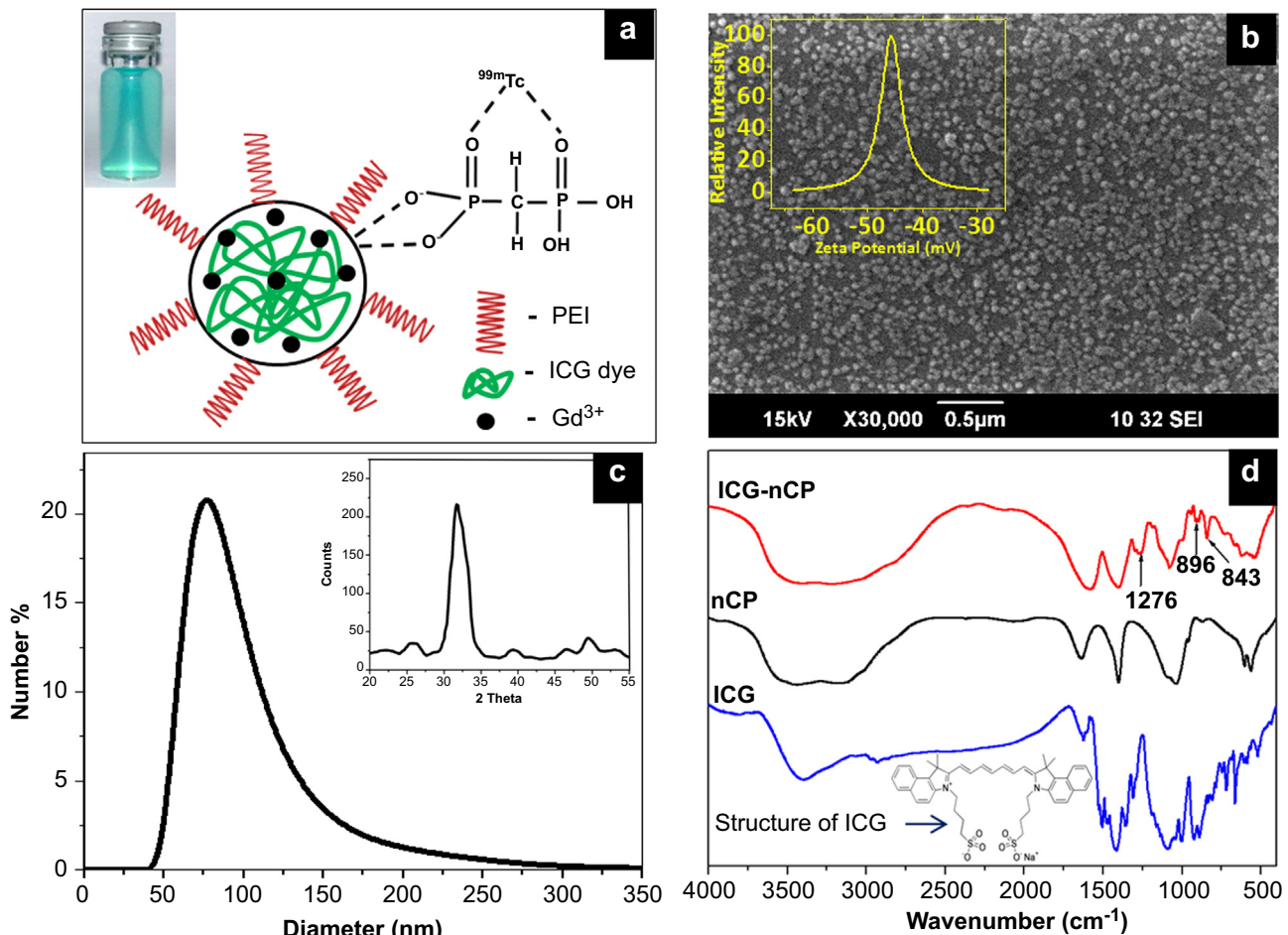


Fig. 1. (a) Schematic of MF-nCP. Inset: solution of MF-nCP (~2 mg/mL). Characterization of MF-nCP: (b) SEM image of MF-nCP. Inset: zeta potential data, (c) DLS data showing particle size distribution. Inset: X-ray diffraction pattern, (d) FTIR data of ICG, nCP and ICG-nCP. Inset: structure of ICG.

from ICG-Gd-nCP. PEI capped ICG-Gd-nCP was then tagged with 99m Tc-MDP to obtain MF-nCP. The schematic of the developed MF-nCP is shown in Fig. 1a. A sample solution of ~ 2 mg/mL MF-nCP is shown as inset of Fig. 1a. The green (in the web version) color of the solution indicates the successful doping of ICG dye within nCP.

Analysis of particle size by SEM imaging showed spherical well dispersed nanoparticles of size ~ 80 nm as seen in Fig. 1b. Zeta potential value of MF-nCP was recorded to be ~ -46 mV (inset of Fig. 1b) which can be attributed to the presence of negatively charged phosphonate groups (MDP) on the surface of the nanoparticles. The size of MF-nCP was further confirmed by DLS that gave a size distribution of 80 ± 30 nm as shown in Fig. 1c. Inset of Fig. 1c shows the XRD data of MF-nCP that exhibited a hydroxyapatite phase with high intensity peak at 31.7° (2 1 1). On comparison with the XRD of highly crystalline HAp phase (JCPDS No. 09-0432), XRD of MF-nCP showed broader and lesser number of peaks indicating that the particles are smaller in size and comparatively amorphous in nature. In order to study the composition of ICG-Gd-nCP, FTIR analysis was carried out. Fig. 1d shows a comparison of the FTIR data of free ICG, bare nCP and ICG-Gd-nCP. As shown in Fig. 1d, ICG-Gd-nCP gave additional peaks at 1276 cm^{-1} , 896 cm^{-1} and 843 cm^{-1} when compared to bare nCP. The band at 1276 cm^{-1} corresponds to aromatic amine group and peaks at 896 cm^{-1} and 843 cm^{-1} corresponds to aromatic C–H group present in ICG. FTIR data confirmed the successful doping of ICG within nCP.

3.2. NIR fluorescence imaging

Different parameters were optimized for the efficient doping of ICG dye within nCP. Although ICG is an FDA approved NIR dye clinically used [44,45], a major limitation is its short plasma half-life of 2–4 min [46]. Therefore, a number of nanoparticle-based carriers for ICG have been designed that provide an improved stability [47] and enhanced circulation time [48]. On comparison to polymers and lipids, inorganic matrices such as silica [49] and calcium phosphosilicate [29] served as better nano-carriers for this organic dye.

In our present work, we have investigated the potential of nCP for the entrapment of ICG dye. The optimum doping concentration of ICG was investigated by preparing samples with varying wt% of ICG to nCP (0.05–0.24%). As shown in Fig. 2a, there was an increase in fluorescence emission as ICG doping was varied from 0.05 to 0.15 wt% beyond which the intensity decreased with increased doping. This was also confirmed from the fluorescence intensity graph, Fig. 2b, where the integrated intensity peaked at 0.15 wt%, followed by a decrease in intensity. ICG is an organic dye that tends to aggregate at high concentration leading to fluorescence quenching. Thus, we believe that above an optimum concentration of 0.15 wt%, aggregation of the dye takes place within the nanoparticles leading to fluorescence quenching. The excitation and emission spectrum of 0.15 wt% dye doped ICG-nCP peaked at 765 nm and 800 nm, respectively (Inset: Fig. 2b). These spectral

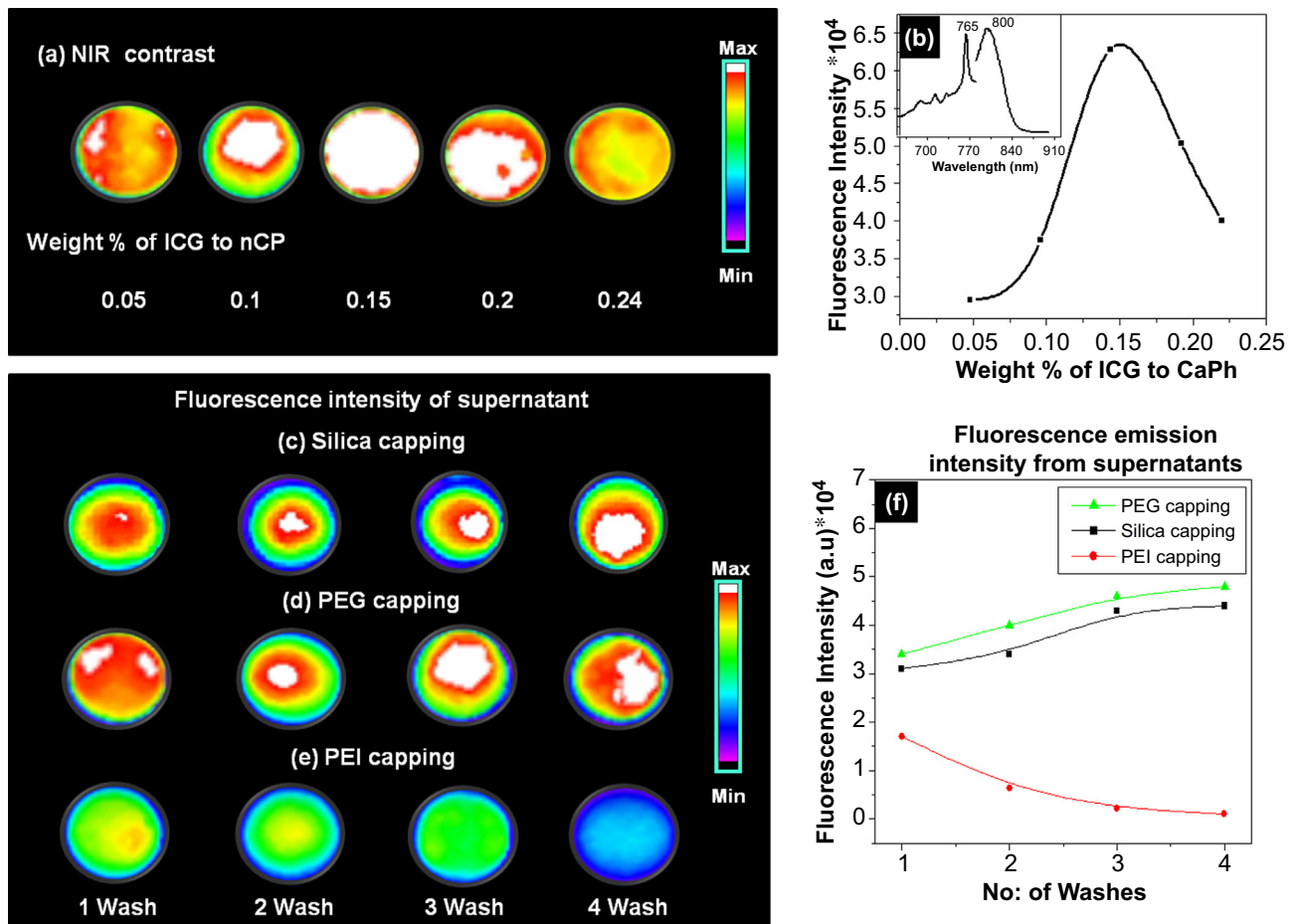


Fig. 2. (a) Fluorescence image of ICG-nCP samples doped with increasing concentrations of ICG, (b) graph showing integrated emission intensity from different batches of ICG-nCP samples. Inset: fluorescence spectra of ICG-nCP. Fluorescence image of the supernatants obtained from subsequent washing of ICG-nCP capped with (c) silica, (d) PEG, (e) PEI, (f) graph showing integrated fluorescence emission from ICG that leached out into the supernatants, on subsequent washing of capped ICG-nCP samples.

features were similar to that of monomeric ICG, confirming that the dye incorporated within the nanoparticles was not aggregated. Compared to our earlier report on crystalline nHAp having an ICG loading efficiency of ~80%, nCP showed an improved efficiency of 90% probably due to its amorphous nature (**Supplementary information: Fig. S1a**). This led to an enhanced fluorescence emission from nCP compared to nHAp which was evident from NIR contrast imaging (**Supplementary information: Fig. S1b**).

Though the dye loading efficiency was high, the major challenge was to avoid leaching-out of ICG from nCP matrix during purification steps and storage. To avoid this, we carried out capping of ICG-nCP with inorganic materials such as silica as well as polymers like PEG and PEI. Efficiency of these capping agents in containing the dye was studied by quantifying the fluorescence intensity of ICG from the supernatants after each washing step. **Fig. 2c–e** shows the NIR fluorescence images of the supernatants collected from silica, PEG or PEI capped ICG-nCP. In case of silica and PEG capping, the fluorescence emission from the supernatants was increasing with each wash, whereas, in case of PEI, emission from the first wash itself was much lower. **Fig. 2f** shows the quantitative fluorescence intensity from the supernatants (of capped samples) after successive washing. Supernatants of PEG and silica capped samples showed almost 50 times higher intensity than the PEI capped sample. Both these data show that ICG is effectively confined within nCP due to PEI capping whereas silica or PEG could not prevent leaching-out of the dye. In order to optimize the concentration of PEI required for effective capping, concentrations varying from 1 to 5×10^{-4} wt% were treated with ICG-nCP. We found that as the concentration of PEI increased from 1×10^{-4} wt% to 5×10^{-4} wt%, at $\sim 2.5 \times 10^{-4}$ wt%, the dye started to remain effectively confined within the nanoparticles without much leaching. On further increasing PEI ($>2.5 \times 10^{-4}$ wt%), agglomeration of nanoparticles took place, which could be observed visually (data not shown). This might have occurred due to the cross linking of ICG-nCP by the polymer. Thus the optimum concentration of PEI required to prevent ICG leaching was identified as $\sim 2.5 \times 10^{-4}$ wt%. In certain

recent reports, the efficiency of PEI for capping nCP was discussed [50]. Probably in the present case, the adsorption of PEI on the surface of nCP and the electrostatic interaction between the primary, secondary and tertiary amine groups present in PEI with the free sulphonate groups of ICG helped the polymer to provide a protective coating for ICG-nCP.

3.3. Magnetic contrast imaging of MF-nCP

Gd^{3+} was doped into ICG-nCP (0.15 wt% ICG containing sample), in order to bring in paramagnetic property required for T_1 weighted bright contrast. The feasibility of co-doping ICG and Gd^{3+} into crystalline hydroxyapatite nanoparticle was discussed in our earlier report [41] and we have followed similar doping methods for amorphous nCP as well. Different batches of Gd^{3+} doped samples were prepared by varying doping concentration from 0.68 to 11.25 at% (ICP data). MR signal intensity from the doped samples (1 mg/mL) was then analyzed using T_1 FLASH imaging protocol. As shown in **Fig. 3a**, with increase in Gd^{3+} from 0.68 to 3.38 at%, the MR contrast increased up to 3.38 at%, beyond which the intensity started diminishing. Further, the variation in T_1 contrast with change in nanoparticle concentration for a fixed Gd^{3+} (3.38 at%) was also studied. As shown in **Fig. 3b**, there was an increase in the MR signal intensity up to 2 mg/mL, but decreased toward 5 mg/mL. To better understand this behavior we have measured both T_1 and T_2 relaxation times with varied Gd^{3+} doping and concentration of the nanoparticles. **Fig. 3c** shows variation in T_1 relaxation with different material concentration for fixed Gd^{3+} doping percentages. T_1 value was found lowering with increase in Gd^{3+} content as well as with increase nanoparticle concentration. Reduced T_1 is expected to produce brighter MR images, because of enhanced proton exchange with water. Further, the relaxivity (r_1) for 3.38 at% Gd^{3+} doped nCP was calculated to be $\sim 3.25 \text{ mm}^{-1} \text{ s}^{-1}$ as shown in **Fig. 3c** (inset). This is comparable to that of commercially available Gd-DOTA ($3.2 \text{ mm}^{-1} \text{ s}^{-1}$ at 7T) [51]. In case of T_2 relaxation time (**Fig. 3d**), for lower concentration of Gd^{3+} doping (0.68 and 1.35%)

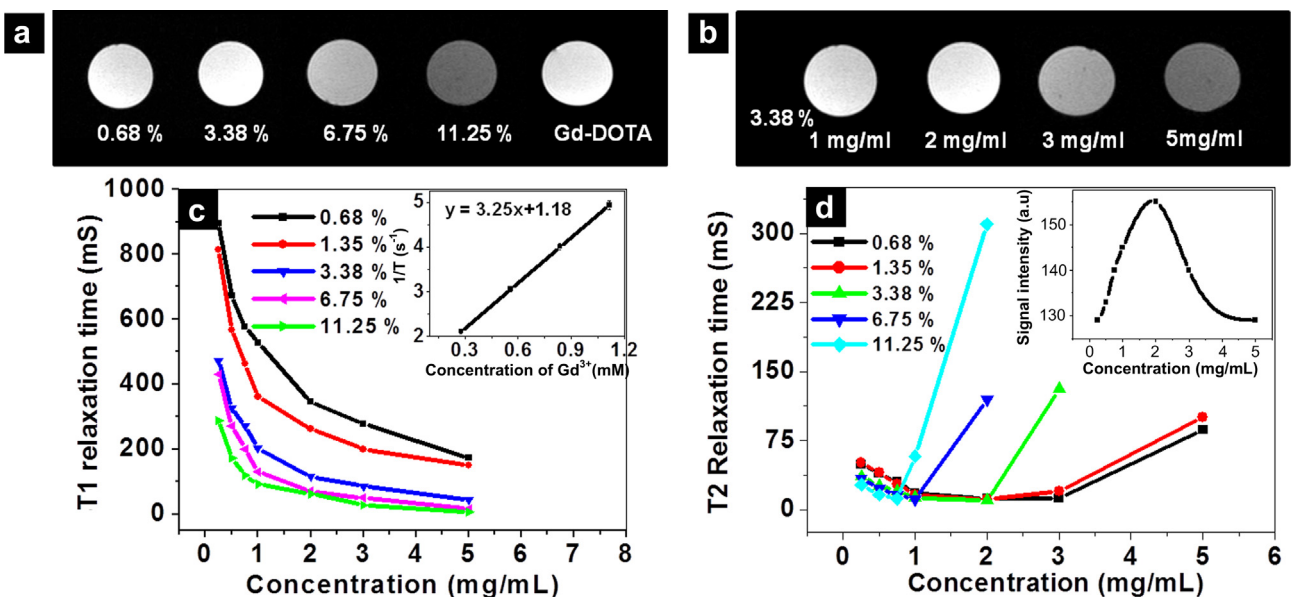


Fig. 3. (a) T_1 weighted magnetic contrast images of 1 mg/mL ICG-nCP samples doped with different atomic percentages of Gd^{3+} , (b) T_1 weighted magnetic contrast image of 3.38% Gd^{3+} doped ICG-nCP, (c) graph showing the variation in T_1 relaxation time of Gd^{3+} doped ICG-nCP at varying doping percentages and concentrations. Inset: relaxivity plot of 3.38% Gd^{3+} doped ICG-nCP (relaxivity value obtained is $3.25 \text{ mm}^{-1} \text{ s}^{-1}$), (d) T_2 relaxation times of Gd^{3+} doped ICG-nCP at varying doping percentages and concentrations. Inset: T_1 weighted MR signal intensity variation of 3.38% Gd^{3+} doped ICG-nCP at varying concentration. The reduction in intensity after 2 mg/mL can be correlated to rapid increase in T_2 values after 2 mg/mL (green color). (For interpretation of the references to color in this figure legend, the reader is referred to the web version of this article.)

the T_2 value changed marginally with the concentration of nanoparticles. However, above 3.38% there was abrupt increase in T_2 relaxation time with nanoparticles concentration (Fig. 3d). In case of 11.25% sample, T_2 shoot-up at < 1 mg/mL. This means, although T_1 was reducing with doping, which should render brighter MR images, strong T_2 influence was dominating in all samples at higher Gd^{3+} concentration resulting in darker contrast above 2 mg/mL (Fig. 3b, Inset Fig. 3d). This also explains the reduction in bright contrast seen in Fig. 3a for 6.75 and 11.25% Gd^{3+} samples at 1 mg/mL. Such observations of T_2 based negative contrast were also seen in other Gd based nano-contrast agents [51]. This could be explained based on the chemical exchange model applied to weakly magnetized particles at high magnetic field strength [52]. The T_2 relaxation time of such particles depends on the proton exchange between water just surrounding the particle and the bulk. Gd^{3+} doped within the nanoparticles may act as paramagnetic centers that create a gradient leading to effective T_2 shortening in a high magnetic field [51]. In addition, the nano-size and porous nature of amorphous calcium phosphate may help in the better interaction between protons and doped Gd^{3+} . At higher doping, there can be clustering of Gd^{3+} within nCP as we have seen in our earlier studies on Eu^{3+} and Gd^{3+} co-doped nHAp [38]. Such Gd clusters may act as T_2 centers rendering negative contrast. From the above results, it is clear that an optimum doping % of Gd^{3+} as well as nanoparticles concentration was required to obtain bright T_1 contrast. Considering the best contrast properties observed, we have selected 3.38 at% Gd^{3+} doped nCP for further *in vivo* testing. As estimated from the ICP data, this material will contain $\sim 45 \times 10^5$ Gd^{3+} ions per nanoparticle of size ~ 80 nm. This was comparable to that of Gd^{3+} doped silica contrast agent, reported recently by Jokerst et al., for multimodal imaging of human mesenchymal stem cells *in vivo* [15].

One of the major concerns associated with Gd^{3+} doped nano-contrast agents is the possibility of leaching-out of Gd^{3+} from the nanoparticles. This was important to be studied because free Gd^{3+} is reported to cause nephrogenic systemic fibrosis in patients with advanced kidney disease [53]. We have quantified the amount of free Gd^{3+} that leached out from 3.38% Gd^{3+} doped nCP at physiological pH 7.4 and lysosomal pH 4.5. ICP results showed that the amount of free Gd^{3+} that leached out from the nanoparticles at physiological pH (7.4), after 96 h, was below the detectable range. At lysosomal pH of 4.5, $\sim 2.5\%$ of Gd^{3+} leached out in 96 h. This means, from 1 mg of nCP, ~ 4.3 μ g Gd^{3+} may leach out after 96 h under lysosomal pH. In an *in vivo* scenario, if 10 mg/kg nCP is injected to a human being of average weight of 75 kg, ~ 328 μ g of Gd^{3+} may leach out in 96 h. This value is well within acceptable limit and $\sim 10^3$ times lesser compared to the clinically used contrast agent Prohance, where 4.6×10^5 μ g Gd^{3+} leaches out as early as 1.5 h [15]. Thus, 3.38% Gd^{3+} doped nCP is a potential candidate for *in vivo* MR imaging studies.

3.4. Nuclear imaging of MF-nCP

The high affinity of bisphosphonates (BP) to calcium phosphate is being exploited in the field of diagnostics [54] and therapy [55] of bone diseases. BP tagged radionuclides (e.g.: ^{99m}Tc -MDP) are routinely used in bone scintigraphy applications for the diagnosis of bone metastasis, inflammation, fractures and infection [56]. In addition, radionuclide conjugated hydroxyapatite microparticles are used in clinics for therapeutic applications such as radiation synovectomy [57]. But the excellent conjugation of BP to calcium phosphate has not been investigated so far for the development of calcium phosphate based nano-contrast agents. In the present work, we have utilized this opportunity to effectively tag methylene diphosphonate labeled with ^{99m}Tc (^{99m}Tc -MDP) to ICG-Gd-nCP

to develop a multimodal nano-contrast agent. ^{99m}Tc is considered as the most suitable radioisotope for nuclear imaging because of its easy availability, simple conjugation chemistry, short half-life of 6 h and 140 keV gamma emission which is most ideal for the present day Auger cameras.

The concentration of ^{99m}Tc -MDP required to obtain the best labeling efficiency was estimated by treating ~ 20 mg/mL of ICG-Gd-nCP with varying concentrations of ^{99m}Tc (0.01–0.05 ng/mL). Radioactivity of the final washed products and supernatant obtained during washing steps was quantified using a dose calibrator. As shown in Fig. 4a, with increasing concentration of ^{99m}Tc -MDP, there was significant increase in the radioactivity of washed sample from 60 to 250 μ Ci, up to an effective ^{99m}Tc concentration of 0.04 ng/mL, above which saturation was noted. The radioactivity of the corresponding supernatants showed negligible count in the initial concentrations, but it slowly increased above 0.04 ng/mL indicating the presence of unconjugated ^{99m}Tc -MDP molecules (data not shown). The graph in Fig. 4b also depicts the saturation limit at ~ 0.04 ng/mL of ^{99m}Tc above which the radioactivity of the sample remained constant. Thus it is clear that, up to 0.04 ng/mL, all the ^{99m}Tc -MDP molecules got conjugated to ICG-Gd-nCP and above 0.04 ng/mL the excess ^{99m}Tc -MDP remained unreacted. Effective tagging of ^{99m}Tc -MDP was further confirmed by paper chromatography as shown in Fig. 4c. The free ^{99m}Tc -MDP (control) and 0.04 ng/mL ^{99m}Tc labeled ICG-Gd-nCP (hereafter mentioned as MF-nCP) was spotted on the paper chromatograph and after ~ 10 min, free ^{99m}Tc -MDP which is soluble in saline moved along with the solvent whereas MF-nCP remained at the spotted site. The NIR fluorescence from this sample can also be seen at the bottom of the paper. This confirms $\sim 100\%$ tagging efficiency to the nanoparticles. This optimized concentration of radiolabel corresponds to the conjugation of ~ 2 ^{99m}Tc -MDP molecules to each nCP nanoparticle or 0.002 ng ^{99m}Tc /mg of ICG-Gd-nCP. There was a concern whether the presence of PEI on the surface of ICG-Gd-nCP would interfere with its affinity to ^{99m}Tc -MDP. A comparison between the radiolabelling of both PEI capped and uncapped ICG-Gd-nCP (20 mg/mL) was carried out and it was observed that PEI capped particles gave a radioactivity of $\sim 247 \pm 2$ μ Ci whereas uncapped particles gave a value of $\sim 250 \pm 2$ μ Ci. Thus, we concluded that the presence of PEI did not interfere with the radiolabelling of the doped nanoparticles. The stability of the conjugation of ^{99m}Tc -MDP to the nanoparticles was studied by paper chromatography. Fig. 4d,e shows the paper chromatogram of free ^{99m}Tc -MDP on comparison with ^{99m}Tc -MDP tagged nanoparticles at the 0th and 9th hour after incubation with PBS. Even after 9 h there were no signs on free ^{99m}Tc -MDP in the conjugated sample indicating the highly stable radiolabelling of nanoparticles.

3.5. Tri-modal imaging using MF-nCP

After all the experiments regarding contrast optimization, MF-nCP was tested for its simultaneous tri-modal imaging capability under *in vitro* conditions. 3 mg/mL of MF-nCP was suspended in 1% agar and taken in a small tube as shown in Fig. 5a. MF-nCP gave an efficient NIR emission, T_1 based bright magnetic contrast and nuclear emission as shown in Fig. 5b. The sample was then tested for its efficiency to provide tri-modal contrast in a tissue micro-environment, using *ex situ* pork tissue phantoms. MF-nCP (~ 2 mg) was placed within thick pork tissue at ~ 2 cm depth. Fig. 5c shows the experimental setup of a small box filled with pork tissue into which the sample is placed. Fig. 5d–f shows the NIR emission, T_1 based bright magnetic contrast and nuclear contrast from MF-nCP embedded within the tissue. This suggested that all the three contrast properties – optical, magnetic and nuclear – can be

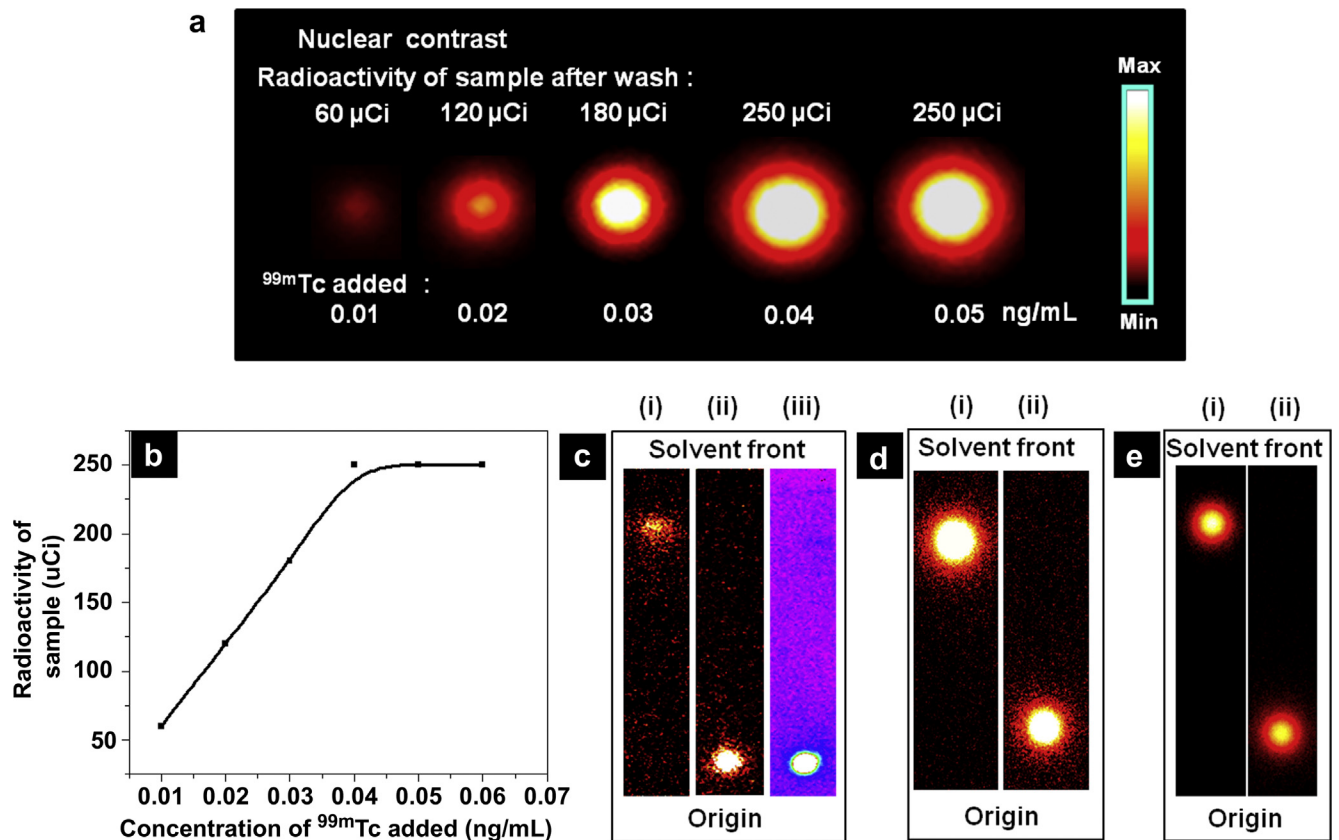


Fig. 4. (a) Nuclear contrast image of ICG-Gd-nCP (20 mg/mL) conjugated with varying concentrations of $^{99\text{m}}\text{Tc}$ -MDP, (b) graphical representation of the amount of radioactivity from the labeled samples as a function of $^{99\text{m}}\text{Tc}$ added during synthesis, (c) paper chromatogram showing (i) radioactive emission from free $^{99\text{m}}\text{Tc}$ -MDP that moved up the paper chromatogram (control), (ii) radioactive emission from 0.04 ng/mL $^{99\text{m}}\text{Tc}$ conjugated ICG-Gd-nCP, (iii) NIR fluorescence from the same sample as in (ii), (d) paper chromatogram of (i) free $^{99\text{m}}\text{Tc}$ -MDP and (ii) washed $^{99\text{m}}\text{Tc}$ conjugated ICG-Gd-nCP soon after incubation, (e) paper chromatogram of (i) free $^{99\text{m}}\text{Tc}$ -MDP and (ii) washed $^{99\text{m}}\text{Tc}$ conjugated ICG-Gd-nCP after incubation for 9 h in PBS.

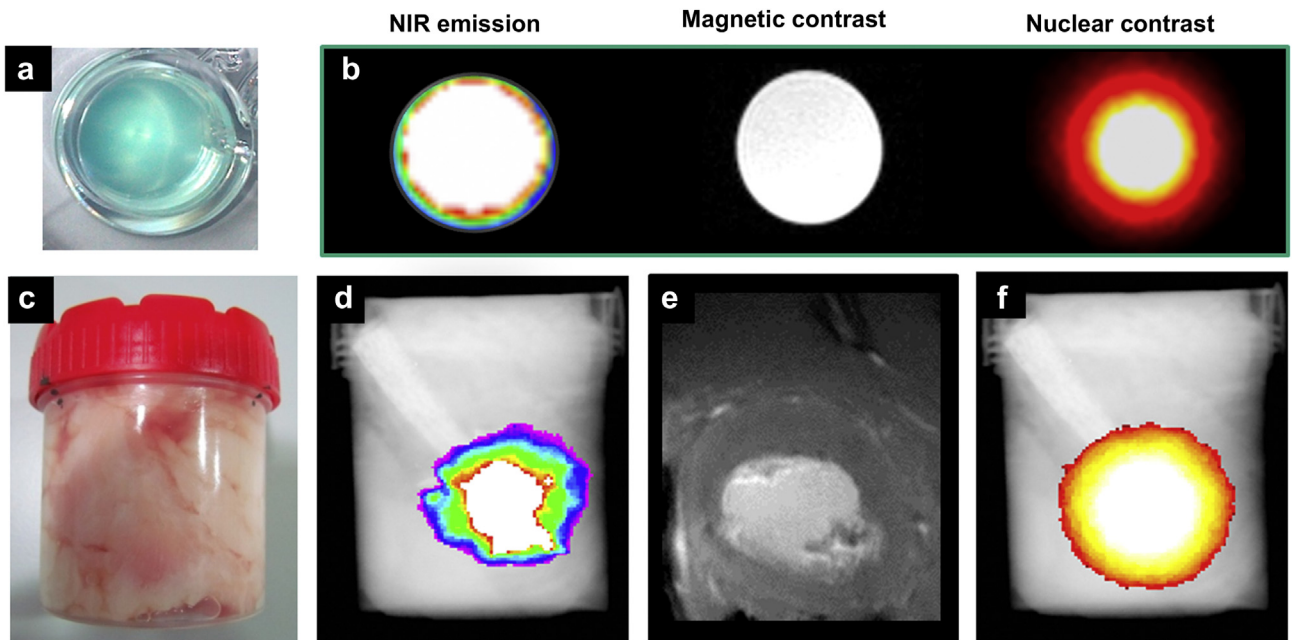


Fig. 5. (a) MF-nCP suspended in agar in a small Eppendorf tube, (b) tri-modal contrast images from MF-nCP showing NIR, magnetic and nuclear contrast. Phantom tissue imaging using MF-nCP: (a) photograph of the experimental setup: container filled with pork tissue in which 2 mg sample is placed at ~2 cm depth within the tissue, (d) NIR fluorescence emission, (e) T_1 weighted magnetic contrast, and (f) nuclear contrast from MF-nCP sample embedded within the tissue.

effectively obtained from the nanoparticles embedded within the tissue micro-environment.

3.6. Hemocompatibility analysis

For clinical applications, most of the nano-contrast agents need to be administrated intravenously and therefore, it is important to understand the blood compatibility of these systems. Recent reports discuss the effect of various parameters such as size [58], composition [59], surface-charge [60] and surface-chemistry [61] on the hemocompatibility of nanoparticles. Therefore, considering the relevance of hematotoxicity analysis, we carried out studies on the effect of MF-nCP on PBMC viability, hemolysis and platelet activation.

3.6.1. Cytotoxicity to PBMC

There are various reports on the activation of immune cells on interaction with nanoparticles [62]. In the present study, the effect of MF-nCP on viability of human immune cells, represented by PBMC, was carried out under *in vitro* conditions. Different concentrations of MF-nCP were treated with PBMC, isolated from the peripheral blood of healthy human subjects, for a time period of 72 h. As seen in Fig. 6a, MF-nCP treated mononuclear cells showed ~100% viability even up to a relatively higher concentration of 500 μ g/mL, indicating excellent compatibility of MF-nCP to immune cells under *in vitro* conditions.

3.6.2. Hemolysis

Hemolysis is the loss of RBC membrane integrity that releases hemoglobin (Hb) into the plasma which can lead to clinical conditions such as hemolytic anemia and hyperbilirubinemia. On intravenous injection, the nanoparticles come into direct contact with RBC and various factors such as the size, charge and surface functionalization of the particles can influence their hemolytic potential [61]. In our study, MF-nCP was treated with whole blood for 3 h and the percentage hemolysis was calculated based on absorption of free Hb in plasma. As shown in Fig. 6b, it was found that MF-nCP does not cause any hemolysis up to a concentration of 250 μ g/mL whereas triton treated whole blood showed ~80% hemolysis. Thus, the study proved that MF-nCP do not affect the membrane integrity of RBC. This was further confirmed by SEM imaging of RBC treated with MF-nCP, PBS and triton. As shown in the inset of Fig. 6b, the intact biconcave shape of RBC was not distorted by treatment with MF-nCP (200 μ g/mL) that was comparable to the shape of RBC treated with PBS (Supplementary Fig. S2a). SEM image of triton treated RBC showed distorted shape confirming the damage on membrane integrity and leakage of Hb (Supplementary Fig. S2b). The above results confirmed the compatibility of MF-nCP toward RBC.

3.6.3. Platelet activation

Platelet activation is one of the initial steps involved in blood clotting which is followed by platelet aggregation and activation of

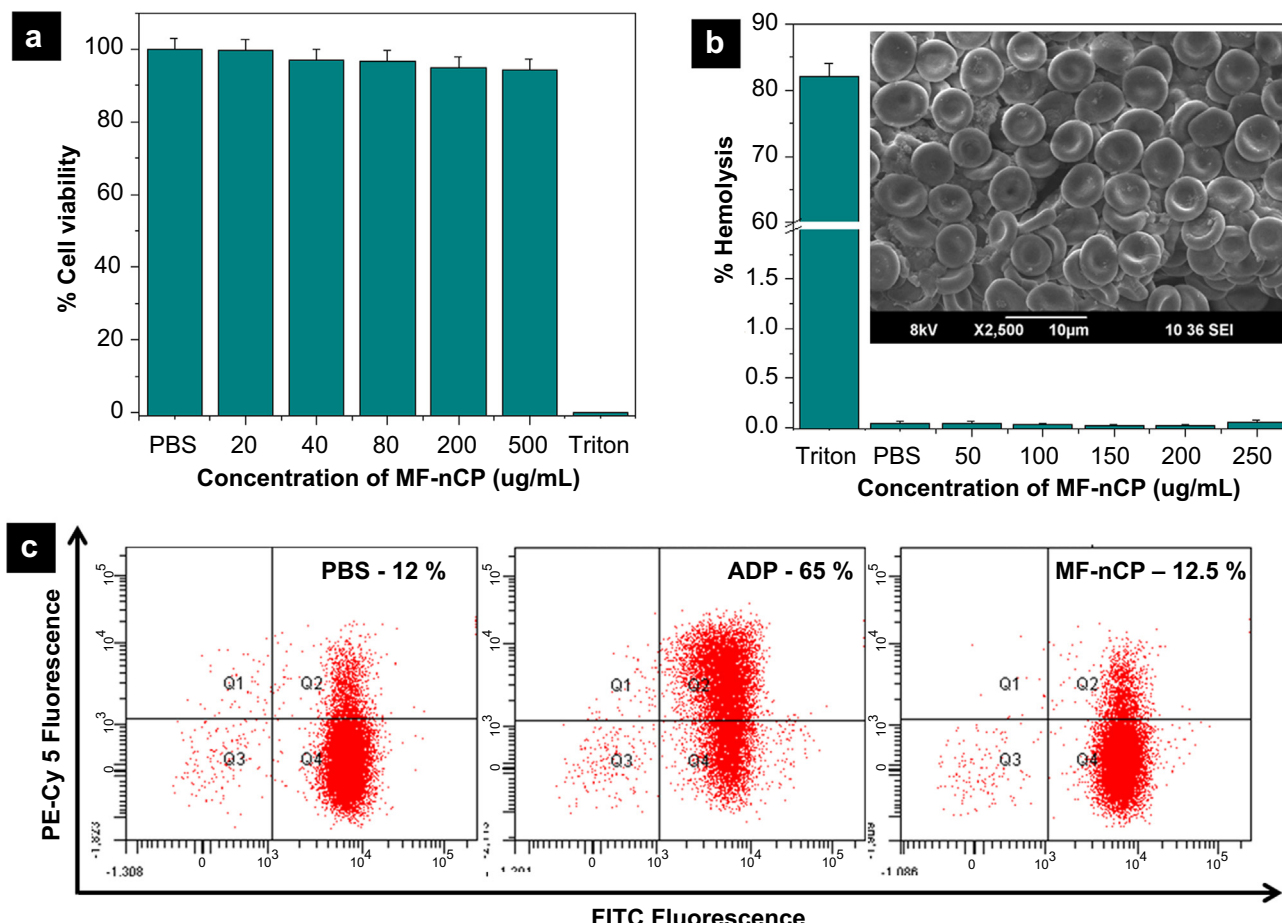


Fig. 6. Hemocompatibility analysis of MF-nCP, (a) cell viability analysis of PBMC treated with MF-nCP for an incubation period of 48 h, (b) hemolysis data of different concentrations of MF-nCP treated with whole blood. Inset: SEM image of RBC treated with MF-nCP (200 μ g/mL), (c) flow cytometry based platelet activation data showing platelets treated with PBS, ADP and 200 μ g/mL MF-nCP.

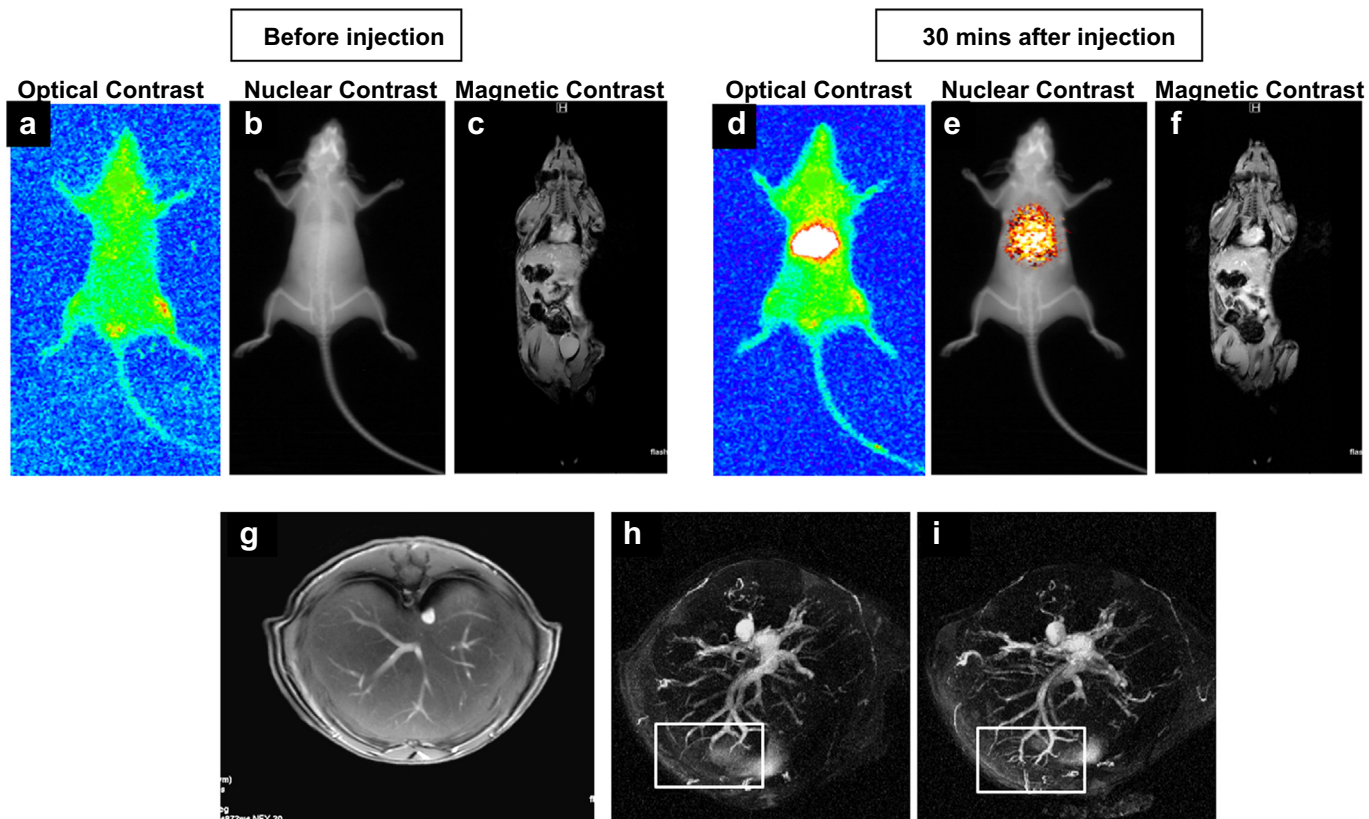


Fig. 7. Tri-modal imaging in Swiss albino mice after tail vein injection of MF-nCP, (a–c) NIR fluorescence image, nuclear emission overlaid over X-ray image and T_1 based MRI before sample injection, (d–f) NIR fluorescence image, radio-emission overlaid on X-ray image and T_1 based MRI of mice 30 min after sample injection, (g) T_1 based MRI of axial liver section 30 min after sample injection. MR angiogram of axial liver sections (h) before and (i) 30 min after injection of MF-nCP. Within the marked region (white rectangular box), the smaller blood vessels are more clearly visible after sample injection.

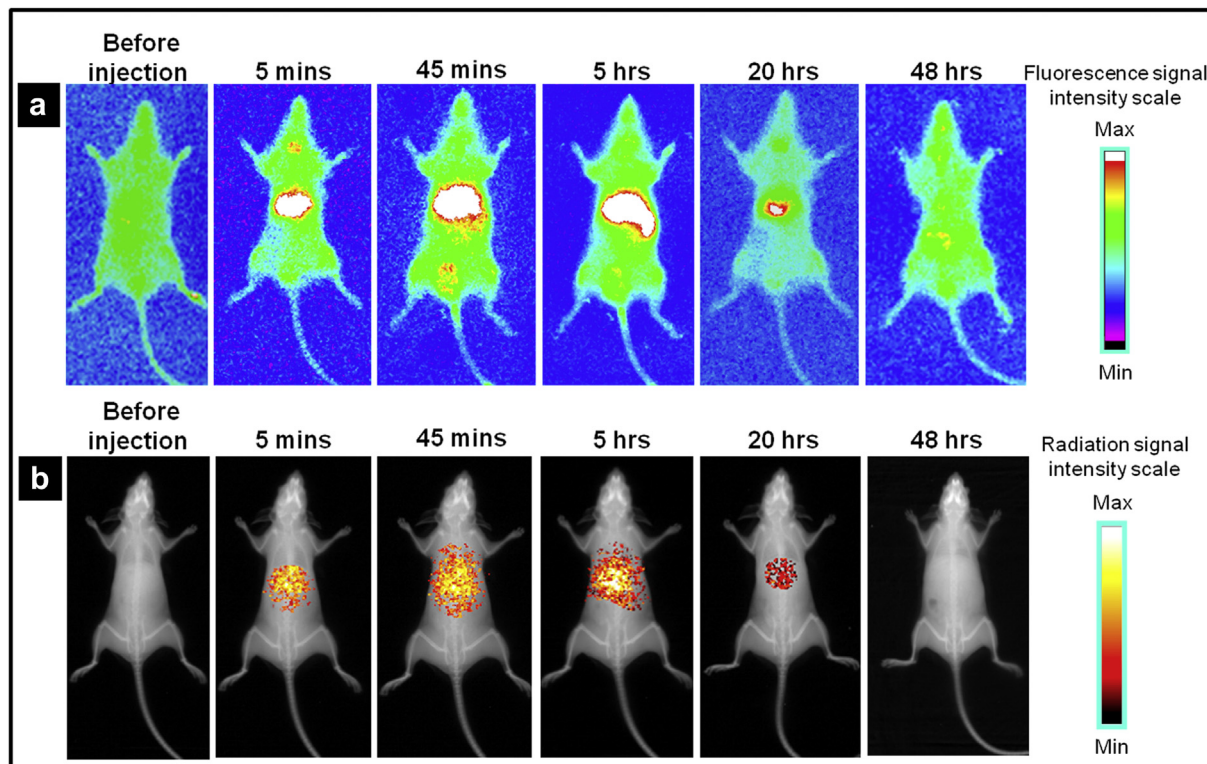


Fig. 8. Biodistribution in Swiss albino mice injected with MF-nCP, (a) NIR fluorescence images, (b) radio-isotopic images from same animals, overlaid on X-ray images.

coagulation factors to form clot. Certain nanoparticles have shown thrombogenic potential that is attributed to their composition, size or charge [63]. The interaction of hydroxyapatite nanoparticles with platelets was reported to cause dense granule secretion or interference with platelet aggregation [64]. This may be due to the dissolution of Ca^{2+} from the hydroxyapatite nanoparticles as the role of Ca^{2+} in platelet activation and aggregation is well reported [65]. Therefore it was important to study the effect of MF-nCP on the activation of platelets. Platelet activation leads to the expression of a number of surface markers. In the present study, expression of CD42b and CD62P were used to identify resting and activated platelets. CD42b or Glycoprotein1b is a resting platelet membrane surface glycoprotein that acts as a receptor for von Willibrand factor whereas CD62P or P-selectin is the most common type of granular membrane protein which is expressed on activated platelets. Therefore, resting platelets expressed CD42b alone whereas activated platelets expressed both CD42b and CD62P. Flow cytometric evaluation was carried out on MF-nCP treated platelets. As shown in Fig. 6c, 12.5% of the platelets treated with MF-nCP showed expression of both CD62P and CD42b. This result was comparable to that of PBS treated platelets that gave an activation of 12% whereas the platelets treated with ADP showed a high activation of 65%. The basal activation of the platelets ($\sim 12\%$) that was observed in both PBS and MF-nCP treated platelets may be due to the *in vitro* experimental conditions. The isotype control data showed that there was no non-specific attachment of the isotypes to the platelets (data not shown). Thus, it was concluded that MF-nCP do not cause any adverse effects on platelet function under

in vitro conditions. Thus, after hematotoxicological evaluation, we have conclusively proved the compatibility of MF-nCP to major blood cell components including mononuclear cells, RBC and platelets suggesting that the contrast agent may be safe for intravenous administration.

3.7. Multimodal *in vivo* imaging and biodistribution analysis in mice models

The *in vivo* tri-modal imaging capability of MF-nCP was investigated in normal adult Swiss albino mice. MF-nCP was administered through tail vein at a concentration of 10 mg/kg. After injection, the animals were imaged for NIR fluorescence, magnetic contrast and radioactive emission. Fig. 7a–c shows NIR fluorescence, T_1 based MRI and nuclear emission overlaid on X-ray image of the mice before sample injection and Fig. 7d–f shows the tri-modal contrast from MF-nCP, 30 min after sample injection. As seen in the figure, bright NIR emission, nuclear signal and T_1 based bright contrast was visible in the liver region, 30 min after sample injection. The radioactive emission was relatively more diffused compared to optical image, indicating the better spatial contrast of optical signals. Fig. 7g shows the axial liver section of the mice 30 min after injection. The blood vessels were clearly visible. The axial liver sections were then chosen for an MR angiogram. Fig. 7h and i shows the MR angiogram before and ~ 30 min after sample injection. As seen in the figure, the smaller blood vessels were more clearly visible after MF-nCP injection (especially the blood vessels inside the white rectangle marked). Further, tracking of

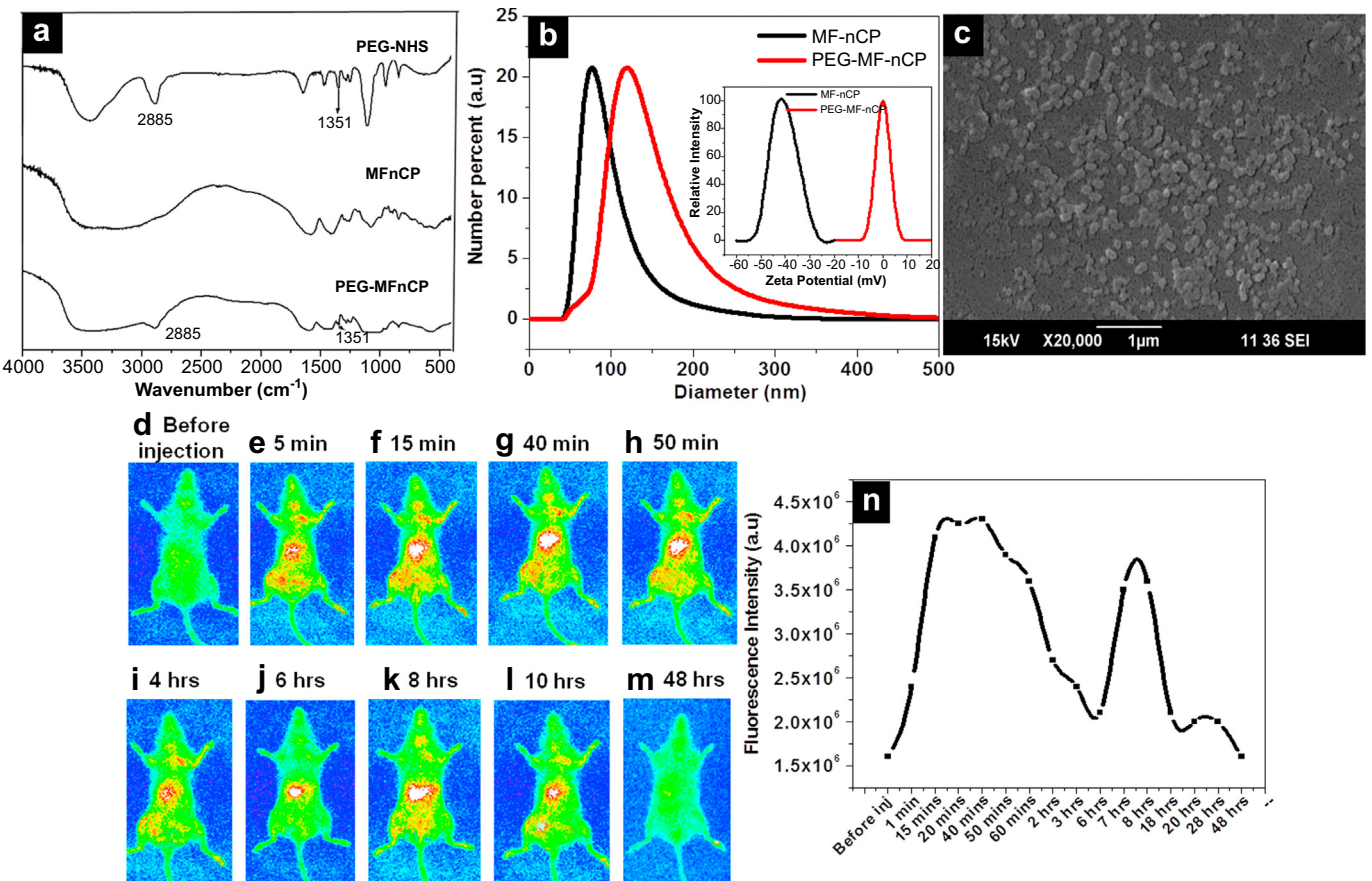


Fig. 9. Characterization of PEG-MF-nCP, (a) FTIR data showing comparison of PEG-MF-nCP, MF-nCP and PEG–NHS. (b) DLS data of PEG-MF-nCP and MF-nCP. Inset: zeta potential of PEG-MF-nCP and MF-nCP, (c) SEM image showing particle size ~ 120 nm, (d–m) *in vivo* fluorescence emission imaging of mice for a period up to 48 h after sample injection, (n) graphical representation of the variation in fluorescence emission in liver with time.

nanoparticles over a period of 48 h is shown in Fig. 8 where NIR fluorescence images (Fig. 8a) and the corresponding radioactive emission overlaid on X-ray image (Fig. 8b) is shown for different time intervals. The slow transition of nanoparticles from the liver to the intestine can be seen during the time interval between 45 min to 5 h. After 20 h, majority of the material was found eliminated from the body and only signals of very low intensity could be seen from the region of liver. After 48 h, the material was found almost completely cleared from the animal body. The biodistribution of free ICG, Gd–DOTA and 99m Tc-MDP was carried out to differentiate their biodistribution from that of MF-nCP (Supplementary Fig. S3a–c). Free ICG was almost completely cleared from the body in 20 h. Free 99m Tc-MDP was cleared through the kidneys in almost 4 h confirming that the radioactive signal obtained from the liver even at the 5th hour is from MF-nCP and not from free 99m Tc-MDP. Gd–DOTA got eliminated from circulation in about 30 min

through the kidneys, which is evident from the T_1 based bright contrast from the bladder.

PEGylation of nanoparticles is known to prolong its blood circulation properties by stearic hindrance which prevents opsonins or immune cells from recognizing the nanoparticles [66]. Considering the relatively extended retention of MF-nCP in liver (~ 5 h), we have PEGylated the samples in order to improve its biodistribution. For this, the amine group of PEI on the surface of MF-nCP was conjugated with NHS activated branched PEG (40 K). The conjugation of PEG to MF-nCP was confirmed using FTIR which gave characteristic peaks of PEG in modified MF-nCP (PEG-MF-nCP) as shown in Fig. 9a. After PEGylation, the size of the nanoparticles increased from 80 nm to 120 nm as shown by the DLS data (Fig. 9b) and SEM image (Fig. 9c). Zeta potential value also changed from -45 mV to -0.03 mV (inset of Fig. 9b). The tri-modal imaging capability of the PEGylated sample was also demonstrated under *in vitro*

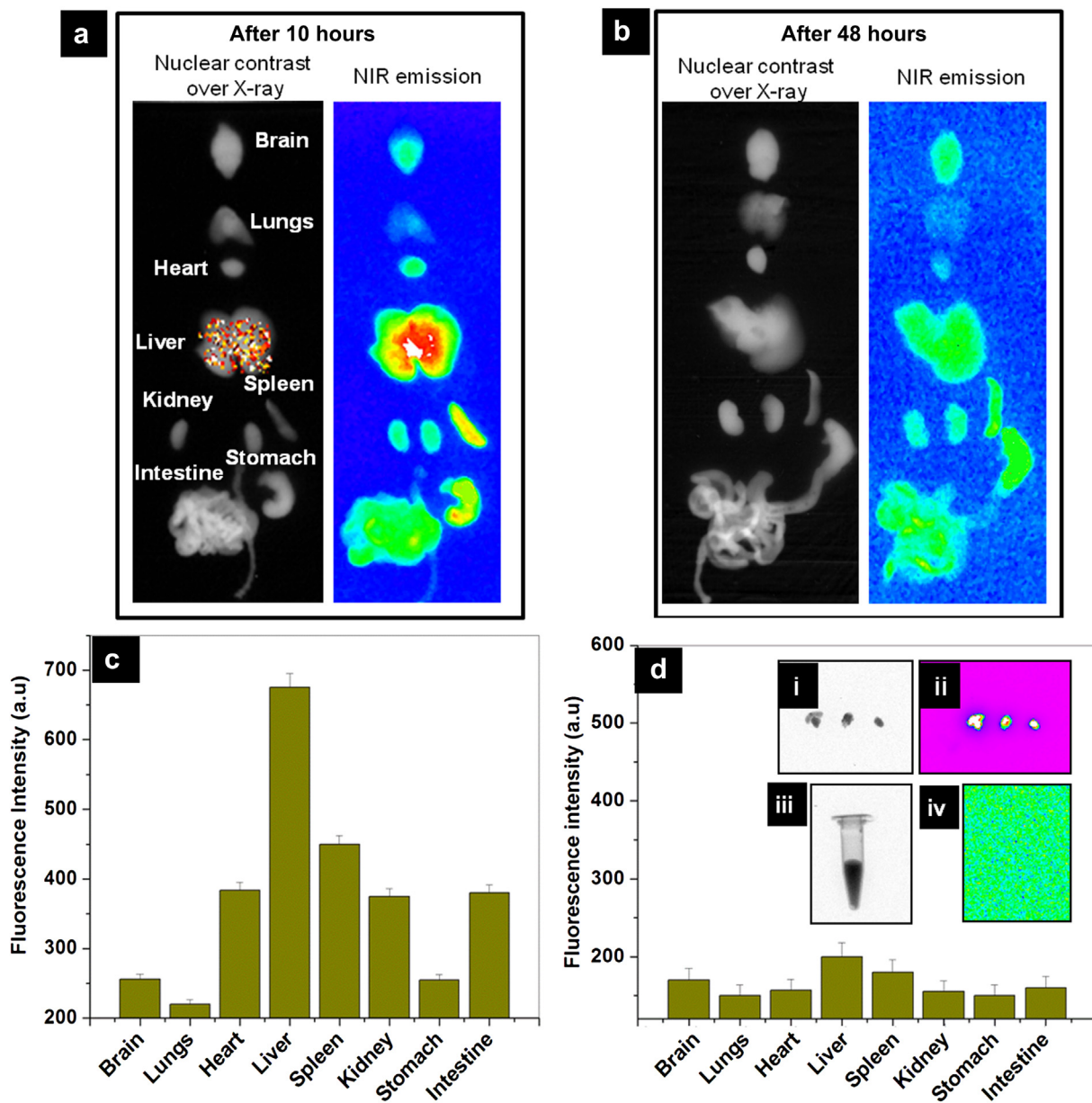


Fig. 10. *Ex-vivo* imaging of the major organs, (a) 10 h after PEG-MF-nCP injection, (b) 48 h after sample injection. Integrated fluorescence emission from different organs, (c) 10 h after sample injection and (d) 48 h after sample injection. Inset of (d): (i) fecal matter collected over a time period of 10–48 h, (ii) corresponding NIR emission image, (iii) urine collected over a period of 10–48 h, (iv) corresponding NIR emission image.

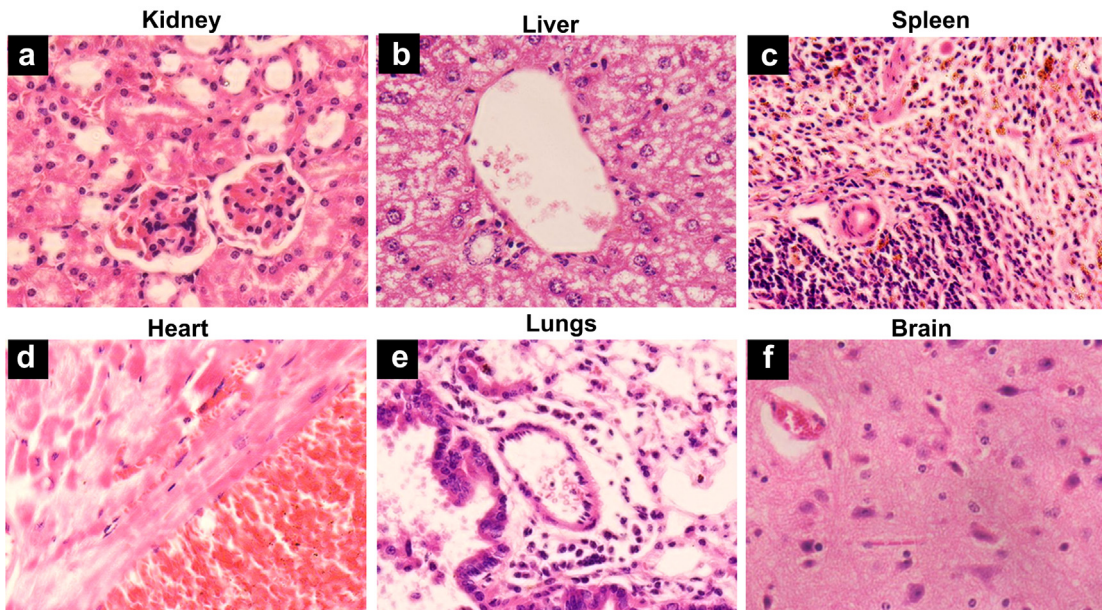


Fig. 11. Histological analysis of (a) kidney, (b) liver, (c) spleen, (d) heart, (e) lungs, (f) brain from mice after 48 h of sample injection at 40 \times magnification showing no changes in the cellular integrity or tissue morphology.

conditions (Supplementary information: Fig. S4a). The hemocompatibility study was repeated for the PEGylated sample which proved its compatibility to mononuclear cells, RBC and platelets (Supplementary information: Fig. S4b–d). Biodistribution of PEG-MF-nCP was carried out in Swiss albino mice as shown in Fig. 9d–m. For convenience, optical contrast images are only shown. Interestingly, there was prolonged circulation for PEGylated nanoparticles and the maximum signal intensity in liver was observed only after 40 min (Fig. 9g). More interestingly, there appeared a re-circulation of these nanoparticles as the intensity from liver reduced after 40 min (Fig. 9h and i), then gradually increased to another peak at \sim 08 h (Fig. 9k) and finally cleared from the body after 48 h (Fig. 9m). The integrated fluorescence emission from the liver at different time intervals (Fig. 9n) also shows this gradual accumulation and re-circulation of nanoparticles before its clearance by 48 h.

Further, the animals were euthanized and organs were imaged to study the relative accumulation of PEG-MF-nCP in different organs. Fig. 10a shows radioactive emission images overlaid on X-ray image and fluorescence emission from the organs collected after \sim 10 h. Fluorescence and radioactive emission could be observed from the liver which correlated well with the *in vivo* imaging studies (Fig. 9). The relative fluorescence emission intensity plot (Fig. 10c) also indicates distribution in various organs with relatively higher signal from liver. There was no significant signal seen from the spleen suggesting no reticuloendothelial system activation. By 48 h, there was no fluorescence or radioactive signals from any of these organs (Fig. 10b), indicating almost complete clearance. Relative fluorescence intensity plot from each organ also confirmed this observation (Fig. 10d). Compared to the urine samples, the fecal matter showed higher fluorescence signal (inset of Fig. 10d) indicating the possible hepatobiliary route of clearance [29]. By 48 h we could observe NIR fluorescence from PEG-MF-nCP in feces sample. Calcium phosphate nanoparticles might not be biodegraded by 48 h because the biodegradation time required for calcium phosphate is at least 2 weeks [67]. Therefore, PEG-MF-nCP might be eliminated through the hepatic route as such without being metabolized or biodegraded.

Histological evaluation of all the major organs, 48 h after sample injection, was carried out by hematoxylin and eosin staining as

shown in Fig. 11. Fig. 11a showed the intact renal corpuscle and bowman's space in the kidney section. The liver section (Fig. 11b) showed intact hepatocytes and central portal vein indicating no pathological changes although relatively high accumulation was found in liver. The section of the spleen (Fig. 11c) showed intact white and red pulp regions. The section of the heart (Fig. 11d) showed intact cardiac muscle and the lung section (Fig. 11e) showed intact alveolar duct and bronchiole. The brain sections also showed intact purkinjee cell layer and granular layer (Fig. 11f). In effect, the histological sections of all major organs did not show any noticeable alteration from the normal anatomy or histology confirming the compatibility of MF-nCP under *in vivo* conditions. Thus, the *in vivo* studies indicate that PEG-MF-nCP is an efficient and non-toxic tri-modal contrast agent with an approximate clearance time of \sim 48 h.

4. Conclusion

We have successfully synthesized a tri-modal contrast agent based on calcium phosphate nanoparticles for combined near-infrared (NIR), magnetic resonance (MR) and nuclear imaging. Doping of nanoparticles (\sim 80 nm) with ICG and Gd³⁺ aided NIR and MR contrast, whereas surface tagging with ^{99m}Tc resulted radioactive emission suitable for nuclear imaging. Surface capping with polyethyleneimine was found critical for confining the organic dye molecules within the amorphous nCP matrix. Studies on hemolytic potential, cytotoxicity to peripheral blood mononuclear cells and platelet activation indicated excellent hemocompatibility of these nanoparticles, which was essential for its intravenous administration for imaging applications. Multimodal imaging carried out in healthy mice models showed the capability of MF-nCP to simultaneously provide excellent near-infrared, magnetic and nuclear contrast under *in vivo* conditions. Immediate accumulation and retention of bare nanoparticles in liver (\sim 5 h) was avoided by PEGylation that provided prolonged blood circulation and periodic redistribution of MF-nCP from the liver. The clearance of PEGylated nanoparticles was observed by \sim 48 h and histology analysis of all major organs showed no pathophysiological changes. Thus, we developed a tri-modal contrast agent using calcium phosphate

nanoparticles and demonstrated its potential for combined NIR, MR and nuclear imaging *in vivo*. This type of tri-modal contrast agents may facilitate the merging of high spatial resolution and sensitivity of optical signals with clear anatomical and functional details through MRI and detailed physiological information from nuclear imaging.

Acknowledgment

Authors thank, Department of Biotechnology (DBT), Govt of India for financial support under the project “*In silico* design, development, nanotoxicology and preclinical evaluation of theragnostic cancer nanomedicine – Phase II” (BT/PR14920/NNT/28/503/2010). Authors thank Department of Science and Technology (DST) for financial support under the project “Theragnostics, Regenerative Medicine and Stem Cell Research using Cell-Targeted Nanomaterials” (SR/NM/NS-99/2009). AA is thankful to CSIR for Senior Research Fellowship (9/963(0016)2K11-EMRI). Authors thank Mr. Sajin P. Ravi for his support in scanning electron microscopy and Mrs. Sreerekha P. R. for FACS analysis. Authors also thank Mr. Sunil Kumar O.R for his technical assistance in the animal experiments. Authors thank Sophisticated Test and Information Centre, CUSAT, Kerala for ICP-AES analysis.

Appendix A. Supplementary data

Supplementary data related to this article can be found at <http://dx.doi.org/10.1016/j.biomaterials.2013.05.077>.

References

- [1] Moore A, Medarova Z, Potthast A, Dai G. In vivo targeting of underglycosylated MUC-1 tumor antigen using a multimodal imaging probe. *Cancer Res* 2004;64:1821–7.
- [2] Kircher MF, Mahmood U, King RS, Weissleder R, Josephson L. A multimodal nanoparticle for preoperative magnetic resonance imaging and intraoperative optical brain tumor delineation. *Cancer Res* 2003;63:8122–5.
- [3] Josephson L, Kircher MF, Mahmood U, Tang Y, Weissleder R. Near-infrared fluorescent nanoparticles as combined MR/optical imaging probes. *Bioconjug Chem* 2002;13:554–60.
- [4] Cheng L, Yang K, Li Y, Zeng X, Shao M, Lee ST, et al. Multifunctional nanoparticles for upconversion luminescence/MR multimodal imaging and magnetically targeted photothermal therapy. *Biomaterials* 2012;33:2215–22.
- [5] Bar-Shalom R, Yefremov N, Guralnik L, Gaitini D, Frenkel A, Kuten A, et al. Clinical performance of PET/CT in evaluation of cancer: additional value for diagnostic imaging and patient management. *J Nucl Med* 2003;44:1200–9.
- [6] Israel O, Kuten A. Early detection of cancer recurrence: 18F-FDG PET/CT can make a difference in diagnosis and patient care. *J Nucl Med* 2007;48:28S–35.
- [7] Beyer T, Townsend DW, Brun T, Kinahan PE, Charron M, Roddy R, et al. A combined PET/CT scanner for clinical oncology. *J Nucl Med* 2000;41:1369–79.
- [8] Judenhofer MS, Wehrli HF, Newport DF, Catana C, Siegel SB, Becker M, et al. Simultaneous PET–MRI: a new approach for functional and morphological imaging. *Nat Med* 2008;14:459–65.
- [9] Buchbender C, Heusner TA, Lauenstein TC, Bockisch A, Antoch G. Oncologic PET/MRI, part 1: tumors of the brain, head and neck, chest, abdomen, and pelvis. *J Nucl Med* 2012;53:928–38.
- [10] Becker A, Hessenius C, Licha K, Ebert B, Sukowski U, Semmler W, et al. Receptor-targeted optical imaging of tumors with near-infrared fluorescent ligands. *Nat Biotechnol* 2001;19:327–31.
- [11] Xu H, Cheng L, Wang C, Ma X, Li Y, Liu Z. Polymer encapsulated upconversion nanoparticle/iron oxide nanocomposites for multimodal imaging and magnetic targeted drug delivery. *Biomaterials* 2011;32:9364–73.
- [12] Mulder WJ, Koole R, Brandwijk RJ, Storm G, Chin PT, Strijkers GJ, et al. Quantum dots with a paramagnetic coating as a bimodal molecular imaging probe. *Nano Lett* 2006;6:1–6.
- [13] Mitchell N, Kalber TL, Cooper MS, Sunassee K, Chalker SL, Shaw KP, et al. Incorporation of paramagnetic, fluorescent and PET/SPECT contrast agents into liposomes for multimodal imaging. *Biomaterials* 2013;34:1179–92.
- [14] Huang X, Zhang F, Lee S, Swierczewska M, Kiesewetter DO, Lang L, et al. Long-term multimodal imaging of tumor draining sentinel lymph nodes using mesoporous silica-based nanoprobes. *Biomaterials* 2012;33:4370–8.
- [15] Jokerst JV, Khademi C, Gambhir SS. Intracellular aggregation of multimodal silica nanoparticles for ultrasound-guided stem cell implantation. *Sci Transl Med* 2013;5:177ra35.
- [16] Selvan ST, Patra PK, Ang CY, Ying JY. Synthesis of silica-coated semiconductor and magnetic quantum dots and their use in the imaging of live cells. *Angew Chem Int Ed Engl* 2007;46:2448–52.
- [17] Derfus AM, Chan WCW, Bhatia SN. Probing the cytotoxicity of semiconductor quantum dots. *Nano Lett* 2004;4:11–8.
- [18] Napierska D, Thomassen LC, Rabolli V, Lison D, Gonzalez L, Kirsch-Volders M, et al. Size-dependent cytotoxicity of monodisperse silica nanoparticles in human endothelial cells. *Small* 2009;5:846–53.
- [19] Avnir D, Levy D, Reisfeld R. The nature of the silica cage as reflected by spectral changes and enhanced photostability of trapped rhodamine 6G. *J Phys Chem* 1984;88:5956–9.
- [20] Edwards WB, Akers WJ, Ye Y, Cheney PP, Bloch S, Xu B, et al. Multimodal imaging of integrin receptor-positive tumors by bioluminescence, fluorescence, gamma scintigraphy, and single-photon emission computed tomography using a cyclic RGD peptide labeled with a near-infrared fluorescent dye and a radionuclide. *Mol Imaging* 2009;8:101–10.
- [21] Bhushan KR, Misra P, Liu F, Mathur S, Lenkinski RE, Frangioni JV. Detection of breast cancer microcalcifications using a dual-modality SPECT/NIR fluorescent probe. *J Am Chem Soc* 2008;130:17648–9.
- [22] Ogawa M, Regino CA, Seidel J, Green MV, Xi W, Williams M, et al. Dual-modality molecular imaging using antibodies labeled with activatable fluorescence and a radionuclide for specific and quantitative targeted cancer detection. *Bioconjug Chem* 2009;20:2177–84.
- [23] Edwards WB, Xu B, Akers W, Cheney PP, Liang K, Rogers BE, et al. Agonist–antagonist dilemma in molecular imaging: evaluation of a monomolecular multimodal imaging agent for the somatostatin receptor. *Bioconjug Chem* 2008;19:192–200.
- [24] Xie J, Chen K, Huang J, Lee S, Wang J, Gao J, et al. PET/NIR/MRI triple functional iron oxide nanoparticles. *Biomaterials* 2010;31:3016–22.
- [25] Cai W, Wu Y, Chen K, Cao Q, Tice DA, Chen X. In vitro and *in vivo* characterization of 64Cu-labeled Abegrin, a humanized monoclonal antibody against integrin alpha v beta 3. *Cancer Res* 2006;66:9673–81.
- [26] Hwang do W, Ko HY, Lee JH, Kang H, Ryu SH, Song IC, et al. A nucleolin-targeted multimodal nanoparticle imaging probe for tracking cancer cells using an aptamer. *J Nucl Med* 2010;51:98–105.
- [27] Na HB, Song IC, Hyeon T. Inorganic nanoparticles for MRI contrast agents. *Adv Mater* 2009;21:2133–48.
- [28] Zhou J, Yu M, Sun Y, Zhang X, Zhu X, Wu Z, et al. Fluorine-18-labeled Gd3+/Yb3+/Er3+ co-doped NaYF4 nanophosphors for multimodality PET/MR/UCL imaging. *Biomaterials* 2011;32:1148–56.
- [29] Altinoglu El, Russin TJ, Kaiser JM, Barth BM, Eklund PC, Kester M, et al. Near-infrared emitting fluorophore-doped calcium phosphate nanoparticles for *in vivo* imaging of human breast cancer. *ACS Nano* 2008;2:2075–84.
- [30] Mondejar SP, Kovtun A, Epple M. Lanthanide-doped calcium phosphate nanoparticles with high internal crystallinity and with a shell of DNA as fluorescent probes in cell experiments. *J Mater Chem* 2007;17:4153–9.
- [31] Kester M, Heakal Y, Fox T, Sharma A, Robertson GP, Morgan TT, et al. Calcium phosphate nanocomposite particles for *in vitro* imaging and encapsulated chemotherapeutic drug delivery to cancer cells. *Nano Lett* 2008;8:4116–21.
- [32] Neumann S, Kovtun A, Dietzel ID, Epple M, Heumann R. The use of size-defined DNA-functionalized calcium phosphate nanoparticles to minimize intracellular calcium disturbance during transfection. *Biomaterials* 2009;30:6794–802.
- [33] Sokolova V, Kovtun A, Prymak O, Meyer-Zaika W, Kubareva EA, Romanova EA, et al. Functionalisation of calcium phosphate nanoparticles by oligonucleotides and their application for gene silencing. *J Mater Chem* 2007;17:721–7.
- [34] Dorozhkin SV, Epple M. Biological and medical significance of calcium phosphates. *Angew Chem Int Ed Engl* 2002;41:3130–46.
- [35] He Q, Mitchell AR, Johnson SL, Wagner-Bartak C, Morcol T, Bell SJ. Calcium phosphate nanoparticle adjuvant. *Clin Diagn Lab Immunol* 2000;7:899–903.
- [36] Barth BM, Sharma R, Altinoglu El, Morgan TT, Shanmugavelandy SS, Kaiser JM, et al. Bioconjugation of calcium phosphosilicate composite nanoparticles for selective targeting of human breast and pancreatic cancers *in vivo*. *ACS Nano* 2010;4:1279–87.
- [37] Barth BM, Altinoglu E, Shanmugavelandy SS, Kaiser JM, Crespo-Gonzalez D, DiVittore NA, et al. Targeted indocyanine-green-loaded calcium phosphosilicate nanoparticles for *in vivo* photodynamic therapy of leukemia. *ACS Nano* 2011;5:5325–37.
- [38] Ashokan A, Menon D, Nair S, Koyakutty M. A molecular receptor targeted, hydroxyapatite nanocrystal based multi-modal contrast agent. *Biomaterials* 2010;31:2606–16.
- [39] Chen F, Huang P, Zhu YJ, Wu J, Cui DX. Multifunctional Eu3+/Gd3+ dual-doped calcium phosphate vesicle-like nanospheres for sustained drug release and imaging. *Biomaterials* 2012;33:6447–55.
- [40] Chen F, Huang P, Zhu YJ, Wu J, Zhang CL, Cui DX. The photoluminescence, drug delivery and imaging properties of multifunctional Eu3+/Gd3+ dual-doped hydroxyapatite nanorods. *Biomaterials* 2011;32:9031–9.
- [41] Ashokan A, Chandran P, Sadanandan AR, Koduri CK, Retnakumari AP, Menon D, et al. Development and haematotoxicological evaluation of doped hydroxyapatite based multimodal nanonanoparticle for near-infrared, magnetic resonance and X-ray contrast imaging. *Nanotoxicology* 2012;6:652–66.
- [42] Hu YY, Rawal A, Schmidt-Rohr K. Strongly bound citrate stabilizes the apatite nanocrystals in bone. *Proc Natl Acad Sci USA* 2010;107:22425–9.
- [43] Xie B, Nancollas GH. How to control the size and morphology of apatite nanocrystals in bone. *Proc Natl Acad Sci USA* 2010;107:22369–70.

- [44] Cherrick GR, Stein SW, Leevy CM, Davidson CS. Indocyanine green: observations on its physical properties, plasma decay, and hepatic extraction. *J Clin Invest* 1960;39:592–600.
- [45] Ntziachristos V, Yodh AG, Schnall M, Chance B. Concurrent MRI and diffuse optical tomography of breast after indocyanine green enhancement. *Proc Natl Acad Sci USA* 2000;97:2767–72.
- [46] Landsman ML, Kwant G, Mook GA, Zijlstra WG. Light-absorbing properties, stability, and spectral stabilization of indocyanine green. *J Appl Physiol* 1976;40:575–83.
- [47] Saxena V, Sadoqi M, Shao J. Enhanced photo-stability, thermal-stability and aqueous-stability of indocyanine green in polymeric nanoparticulate systems. *J Photochem Photobiol B* 2004;74:29–38.
- [48] Saxena V, Sadoqi M, Shao J. Polymeric nanoparticulate delivery system for Indocyanine green: biodistribution in healthy mice. *Int J Pharm* 2006;308:200–4.
- [49] Lee CH, Cheng SH, Wang YJ, Chen YC, Chen NT, Souris J, et al. Near-Infrared mesoporous silica nanoparticles for optical imaging: characterization and in vivo biodistribution. *Adv Funct Mater* 2009;19:215–22.
- [50] Shkilnyy A, Friedrich A, Tiersch B, Schöne S, Fechner M, Koetz J, et al. Poly(ethylene imine)-controlled calcium phosphate mineralization. *Langmuir* 2008;24:2102–9.
- [51] Yeh CS, Su CH, Ho WY, Huang CC, Chang JC, Chien YH, et al. Tumor targeting and MR imaging with lipophilic cyanine-mediated near-infrared responsive porous Gd silicate nanoparticles. *Biomaterials* 2013;34:5677–88.
- [52] Brooks RA, Moiny F, Gillis P. On T2-shortening by weakly magnetized particles: the chemical exchange model. *Magn Reson Med* 2001;45:1014–20.
- [53] Hope TA, Herfkens RJ, Denianke KS, LeBoit PE, Hung YY, Weil E. Nephrogenic systemic fibrosis in patients with chronic kidney disease who received gadopentetate dimeglumine. *Invest Radiol* 2009;44:135–9.
- [54] Even-Sapir E, Martin RH, Barnes DC, Pringle CR, Iles SE, Mitchell MJ. Role of SPECT in differentiating malignant from benign lesions in the lower thoracic and lumbar vertebrae. *Radiology* 1993;187:193–8.
- [55] Flanagan AM, Chambers TJ. Inhibition of bone resorption by bisphosphonates: interactions between bisphosphonates, osteoclasts, and bone. *Calcif Tissue Int* 1991;49:407–15.
- [56] Love C, Din AS, Tomas MB, Kalapparambath TP, Palestro CJ. Radionuclide bone imaging: an illustrative review. *Radiographics* 2003;23:341–58.
- [57] Santos MF, Furtado RN, Konai MS, Castiglioni ML, Marchetti RR, Natour J. Effectiveness of radiation synovectomy with samarium-153 particulate hydroxyapatite in rheumatoid arthritis patients with knee synovitis: a controlled randomized double-blind trial. *Clinics* 2009;64:1187–93.
- [58] Mayer A, Vadon M, Rinner B, Novak A, Wintersteiger R, Fröhlich E. The role of nanoparticle size in hemocompatibility. *Toxicology* 2009;258:139–47.
- [59] Tiwari DK, Jin T, Behari J. Dose-dependent in-vivo toxicity assessment of silver nanoparticle in Wistar rats. *Toxicol Mech Methods* 2011;21:13–24.
- [60] Jevprasesphant R, Penny J, Jalal R, Attwood D, McKeown NB, D'Emanuele A. The influence of surface modification on the cytotoxicity of PAMAM dendrimers. *Int J Pharm* 2003;252:263–6.
- [61] Wang W, Xiong W, Zhu Y, Xu H, Yang X. Protective effect of PEGylation against poly(amidoamine) dendrimer-induced hemolysis of human red blood cells. *J Biomed Mater Res B Appl Biomater* 2010;93:59–64.
- [62] Chen BX, Wilson SR, Das M, Coughlin DJ, Erlanger BF. Antigenicity of fullerenes: antibodies specific for fullerenes and their characteristics. *Proc Natl Acad Sci USA* 1998;95:10809–13.
- [63] Radomski A, Jurasz P, Alonso-Escalona D, Drews M, Morandi M, Malinski T, et al. Nanoparticle-induced platelet aggregation and vascular thrombosis. *Br J Pharmacol* 2005;146:882–93.
- [64] Miller VM, Hunter LW, Chu K, Kaul V, Squillace PD, Lieske JC, et al. Biologic nanoparticles and platelet reactivity. *Nanomedicine (Lond)* 2009;4:725–33.
- [65] Semerova J, De Paoli Lacerda SH, Simakova O, Holada K, Gelderman MP, Simak J. Carbon nanotubes activate blood platelets by inducing extracellular Ca²⁺ influx sensitive to calcium entry inhibitors. *Nano Lett* 2009;9:3312–7.
- [66] Gabizon A, Catane R, Uziely B, Kaufman B, Safra T, Cohen R, et al. Prolonged circulation time and enhanced accumulation in malignant exudates of doxorubicin encapsulated in polyethylene-glycol coated liposomes. *Cancer Res* 1994;54:987–92.
- [67] Lu J, Descamps M, Dejou J, Koubi G, Hardouin P, Lemaitre J, et al. The biodegradation mechanism of calcium phosphate biomaterials in bone. *J Biomed Mater Res* 2002;63:408–12.